

Spring 5-2016

Prediction of Tonal Acoustic Radiation Due to Feedback-Loop Resonant Interactions in Transitional Airfoils

Seyyed Saman Salehian
Embry-Riddle Aeronautical University

Follow this and additional works at: <https://commons.erau.edu/edt>



Part of the [Aerospace Engineering Commons](#)

Scholarly Commons Citation

Salehian, Seyyed Saman, "Prediction of Tonal Acoustic Radiation Due to Feedback-Loop Resonant Interactions in Transitional Airfoils" (2016). *Doctoral Dissertations and Master's Theses*. 242.
<https://commons.erau.edu/edt/242>

This Thesis - Open Access is brought to you for free and open access by Scholarly Commons. It has been accepted for inclusion in Doctoral Dissertations and Master's Theses by an authorized administrator of Scholarly Commons. For more information, please contact commons@erau.edu.

PREDICTION OF TONAL ACOUSTIC RADIATION DUE TO FEEDBACK-LOOP
RESONANT INTERACTIONS IN TRANSITIONAL AIRFOILS

A Thesis

Submitted to the Faculty

of

Embry-Riddle Aeronautical University

by

Seyyed Saman Salehian

In Partial Fulfillment of the

Requirements for the Degree

of

Master of Science in Aerospace Engineering

May 2016

Embry-Riddle Aeronautical University

Daytona Beach, Florida

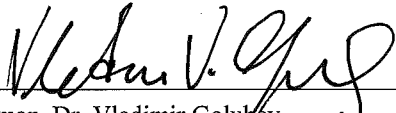
PREDICTION OF TONAL ACOUSTIC RADIATION DUE TO FEEDBACK-LOOP
RESONANT INTERACTIONS IN TRANSITIONAL AIRFOILS

by

Seyyed Saman Salehian

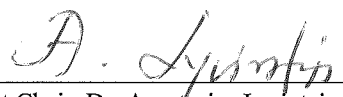
A Thesis prepared under the direction of the candidate's committee chairman, Dr. Vladimir Golubev, Department of Aerospace Engineering, and has been approved by the members of the thesis committee. It was submitted to the School of Graduate Studies and Research and was accepted in partial fulfillment of the requirements for the degree of Master of Science in Aerospace Engineering.

THESIS COMMITTEE

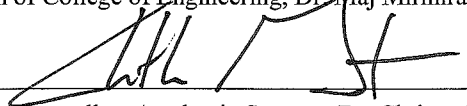

Chairman, Dr. Vladimir Golubev


Member, Dr. Reda Mankbadi


Member, Dr. Anastasios Lyrintzis


Department Chair, Dr. Anastasios Lyrintzis
or Graduate Program Coordinator, Dr. Eric Perrell


Dean of College of Engineering, Dr. Maj Mirmirani


Vice Chancellor, Academic Support, Dr. Christopher Grant

4/28/16
Date

4/28/16
Date

4/28/16
Date

ACKNOWLEDGMENTS

I would like to express deepest gratitude to my advisor Dr. Vladimir Golubev for his support, guidance, understanding, and encouragement throughout my study and research. In addition, I express my appreciation to Dr. Reda Mankbadi and Dr. Anastasios Lyrintzis for having served on my committee. Their thoughtful feedbacks and comments were and still are valued greatly. A special thanks to Aeroacoustics research group at *Ecole Centrale Lyon* for providing experimental data for this research.

I extend my special thanks to my fellow colleagues and friends at PACL lab, Mr. Lap Nguyen and Mr. Marco Sansone for their support throughout this research.

To my family and my dear parents, for their endless love and support.

TABLE OF CONTENTS

LIST OF TABLES	vi
LIST OF FIGURES	vii
SYMBOLS.....	ix
ABBREVIATIONS	x
ABSTRACT.....	xi
1. Introduction	1
1.1. Background.....	1
1.2. Integral Methods.....	3
2. Computational Fluid Dynamics of Near-Field.....	10
2.1. Computational Fluid Dynamics Formulation.....	10
2.2. The Acoustic Field Computation	12
3. Surface Integral Methods Formulations	16
3.1. Surface Integral Formulations	16
3.2. Potential-Theoretic Method (PTM) Formulation	16
3.2.1. Solution Formulation.....	17
3.2.2. Solution Procedure	19
3.2.3. Numerical Procedure.....	23
3.3. Ffowcs Williams – Hawkings (FW-H) Formulation	25
4. Monopole Source Validation	33
5. Far-Field Acoustic Predictions of Transitional Airfoil Noise.....	41
5.1. Near-Field results	41
5.2. Acoustic predictions and comparisons with direct CFD results.....	43
5.3. Acoustic predictions and comparisons with experiment	51
5.4. Tonal acoustic studies of variation of angle of attack	57
6. Conclusions and Recommendations.....	62
REFERENCES	65

LIST OF TABLES

Table 2.1 NACA-0012 Grids employed in 2D and 3D studies.	13
Table 5.1 Far-field peak tonal frequencies by case.....	59

LIST OF FIGURES

Figure 2.1 NACA-0012, Computational Grid.	14
Figure 2.2 NACA-0012, Integration surfaces.	15
Figure 3.1 Problem configuration, Kirchhoff Surface around solid surface.....	18
Figure 3.2 The surface assumed in the FW-H. (Kenneth S and Farassat 1997).....	26
Figure 4.1 The perturbation flow variable contours of the monopole source term.	36
Figure 4.2 Monopole source, Kirchhoff surface, and Observer Location.	36
Figure 4.3 Directivity comparison of PTM at $R=10$ with exact solution for monopole source.	37
Figure 4.4 Directivity comparison of FW-H at $R=10$ with exact solution for monopole source.	37
Figure 4.5 Acoustic pressure RMS directivity at $R=10$ of PTM (Blue) and FW-H (Magenta) with exact solution.	38
Figure 4.6 Error analysis: effect of number of points per wavelength on the surface.	39
Figure 4.7 Error analysis: observer distance to control surface radius ratio (R/r).	40
Figure 5.1 Velocity field obtained from CFD, superimposed with the control surfaces. .	42
Figure 5.2 Pressure waves contour obtained from CFD	42
Figure 5.3 Acoustic spectra at $R/c = 5$ and $\theta = 90^\circ$ using S1, S2, and S3 surfaces in Log scale.....	43
Figure 5.4 Acoustic spectra at $R/c = 5$ and $\theta = 90^\circ$ using S1, S2, and S3 surfaces obtained from PTM.....	44
Figure 5.5 Acoustic spectra at $R/c = 5$ and $\theta = 90^\circ$ using S1, S2, and S3 surfaces obtained from FW-H.....	44
Figure 5.6 Peak tone directivity at $R/c = 5$ using S1, S2, and S3 surfaces obtained from PTM	45
Figure 5.7 RMS directivity at $R/c = 5$ by S1, S2, and S3 surfaces obtained from FW-H	46
Figure 5.8 RMS pressure variations in radial direction computed from CFD simulations	47
Figure 5.9 Peak tone directivity at $R/c = 5$ using S1, S2, and S3 surfaces obtained from FW-H	47
Figure 5.10 RMS directivity at $R/c = 5$ using S1, S2, and S3 surfaces obtained from FW-H	48
Figure 5.11 Peak and RMS directivity at $R/c = 5$ using S3 surface	49
Figure 5.12 Time history and Fast Fourier transform of lift and drag coefficients	50
Figure 5.13 Peak tone sound pressure level in terms of directivity angle.	51

Figure 5.14 Acoustic Spectrum at $R/c = 12.5$ (PTM) without Correction	52
Figure 5.15 Acoustic Spectrum at $R/c = 12.5$ (PTM) with Correction	52
Figure 5.16 Acoustic Spectrum at $R/c = 12.5$ two dimensional and span averaged three dimensional data employed for PTM method and comparison with Experiment	54
Figure 5.17 Acoustic Spectrum at $R/c = 12.5$ two dimensional and span averaged three dimensional data employed for FW-H method and comparison with Experiment	54
Figure 5.18 Acoustic Spectrum at $R/c = 12.5$ of the long time signal, without averaging (Left) and with averaging (Right)	56
Figure 5.19 Peak tone directivities (Left) and RMS acoustic pressure directivities (Right) from PTM and FW-H methods at the observer radius of $R/c = 12.5$	56
Figure 5.20 Acoustic intensity calculate at S1, S2, S3, S4, and observer circle at $12.5c$.	57
Figure 5.21 Varying angle of attack for fixed $Re = 180,000$ (Arcondoulis et al(Arcondoulis et al. 2013))	58
Figure 5.22 Presence of tones for varied angle of attack	59
Figure 5.23 Far-field acoustic spectra for cases with tonal peaks at $0^\circ, 2^\circ, 4^\circ, 6^\circ$.	60
Figure 5.24 Far-field acoustic spectra for cases without tonal peaks	61

SYMBOLS

u	Tangential velocity
v	Normal velocity
w	Span-wise velocity
\vec{V}	Velocity vector
ρ	Density
T	Temperature
p	Pressure
Re	Reynolds number
S	Control surface
ω	Angular velocity
f	Frequency
c	Chord
p'	Acoustic pressure
G	Green's function
H_n^x	Hankel function
H	Heaviside function
K	Helmholtz number
k	Wave number
M_∞	Free stream Mach number
β_∞	$\sqrt{1 - M_\infty^2}$
σ	Density function
r	Integration surface Radius, for the monopole case
R	Observer circle radius
U	Free stream velocity
F_i	Loading source term
Q	Thickness source term
T_{ij}	Quadrupole source term
c_o	Speed of sound
x, y	Observer coordinates
ξ, η	Source coordinates
\bar{x}, \bar{y}	Transformed distance between observer and source coordinates

ABBREVIATIONS

CFD	Computational Fluid Dynamics
DNS	Direct Numerical Simulation
LES	Large Eddy Simulations
ILES	Implicit Large Eddy Simulations
LEE	Linearized Euler Equations
CAA	Computational Aero-Acoustics
PTM	Potential Theoretic Method
FW-H	Ffowcs Williams and Hawkings
FFT	Fast Fourier Transform
SPL	Sound Pressure Level

ABSTRACT

Salehian, Seyyed Saman MSAE, Embry-Riddle Aeronautical University, May 2016.
Prediction of Tonal Acoustic Radiation Due to Feedback-Loop Resonant Interactions in Transitional Airfoils.

The objective of this work is to employ the surface integral methods to study the far-field noise propagation from the flow acoustic resonant interactions of the transitional airfoil. The Potential-Theoretic Method (PTM) as an advancement to traditional Kirchhoff methods is presented. The PTM eliminates the need to calculate the normal derivatives of pressure and an arbitrary Kirchhoff surface can be employed. The numerical procedure to implement the PTM is fairly simple. The formulation and physical assumptions of the approach is reviewed, and the numerical procedure is implemented. Furthermore, the two dimensional formulation of the Ffowcs Williams - Hawkings (FW-H) equation in frequency, domain is reviewed and then the method is implemented to be used for extending the numerical simulations to far-field evaluations. In order to verify the implemented methods, monopole source verification problem has been studied and the accuracy of the methods is validated. Then, PTM and FW-H methods are used in the transitional airfoil application. The noise generation process of the problem in the near-field is highly nonlinear. Thus, high accuracy 2D simulations based on an Implicit Large Eddy Simulation (ILES) code are conducted for a NACA-0012 airfoil for the Reynolds of 140,000 and zero angle of attack as the baseline case, to obtain the time-dependent flow variables in the near-field. Then the near-field data is passed to the developed PTM and FW-H codes to evaluate the far-field noise acoustics. The predicted acoustic sound pressure level and the directivities are compared with direct

CFD simulation in the mid region where the CFD results are still reliable. Comparing the results, it is deduced that the FW-H is more robust in regards to the choice of control surface. Some remarks about signal processing and properties of the methods are suggested. The acoustic predictions are also evaluated for a far-field microphone probe, to compare them with experimental results. The effects of variations of angle of attack on the tonal noise regime has been studied.

1. Introduction

1.1. Background

In the aerospace industry, aerodynamic noise of an aircraft is usually a very important issue to investigate, because of the need to control or modify the noise. There are many kinds of aerodynamic noise generated from fluids such as jet noise, noise due to unsteady flow around wings, noise due to upstream turbulence and boundary layer separation, and etc. Accurately predicting sound intensities and the noise generation mechanism is crucial to control the noise and subsequently achieve desired compliances with regulations.

The difficulties associated with experimental studies such as high expenses of wind tunnel tests and safety risks in flight tests, have led to numerical simulations as an alternative. The numerical techniques have become more appealing with the continuous evolution of the power and speed of computers. Prediction of aerodynamic noise source using a proper model and employing efficient numerical methods along with investigation of radiation of the noise source is the objective of Computational Aero-Acoustics (CAA). Accurate results in CAA depend heavily upon the full, time-dependent Navier-Stokes equations in order to predict the source of the aerodynamic noise and the propagation of the resulting sound, which has become prevalent in aerospace industry.

Aerodynamically generated sound governed by a nonlinear process can be categorized in two general applications: turbulence generated noise (e.g. jet noise) and impulsive noise due to moving surfaces (e.g. fan noise) (A. Lyrantzis 2003). Turbulence noise cases usually require accurate turbulence models to predict the noise source, while moving surface noise source can be predicted by Euler equations or even full potential

models. Subsequent to the accurate prediction of the sound source, various methods can be incorporated in order to predict the acoustic radiation. The most obvious technique is to extend the full nonlinear computational domain to the far-field location where sound is to be calculated. Sound source (e.g., sound radiating from an airfoil) prediction can be achieved by utilization of direct numerical simulations (DNS), where all scales in the flow field are resolved or large-eddy simulation (LES), in which only the large scale components of turbulence are directly calculated and the unresolved scales are modeled. It is generally accepted that the large scale resolving approaches are more efficient than DNS simulations. The extensive computational memory requirements make direct methods less engaging. Mankbadi et al (Reda R Mankbadi, Hayder, and Povinelli 1994) showed that direct calculation of far-field noise for supersonic jet aeroacoustics problem is not practical. Moreover, Stoker and Smith (Stoker and Smith 1993) mentioned that since the acoustic fluctuations are very small, the use of nonlinear Navier-Stokes equations could cause numerical errors.

As an alternative, the computational domain can be divided into two domains, one governing the nonlinear process of generation of sound source and the other describing the propagation of generated sound source. A review of several methods describing the sound propagation was given by Lyrantzis (A. Lyrantzis 2003).

Using simpler equations to predict the far-field acoustic is one way to avert the prohibitive direct nonlinear Navier-Stokes direct calculations. Instead, the linearized Euler equations (LEE) can be employed to extend the CFD calculations to far-field. In these hybrid methods, the near-field simulations are conducted using high accuracy CFD methods and the extension of solution to mid-field or far-field is evaluated using LEE.

These zonal approaches are more computationally efficient than the direct methods. Furthermore, considering the variable speed of sound outside the near-field region in the LEE calculations, these methods are propitious. Shih et al (Shih, Hixon, and Mankbadi 1997) investigated the sound generation and propagation from a supersonic jet. They utilized large scale filtered compressible Navier-Stokes equations for the unsteady flow in the nonlinear near-field regime and the sound wave propagation in the linear regime was described by linearized Euler equations (Reda R Mankbadi et al. 1995). Du and Morris (Du and Morris 2014) used linearized Euler/Navier-Stokes equations as hybrid methods for jet noise flow. These methods, however, require that a great amount of attention be directed to the minimization of far-field numerical scheme diffusion and dispersion errors and a linear solver is required in the acoustic region.

1.2. Integral Methods

An alternative approach to describe the sound propagation in the far-field is the acoustic analogy. The complete Navier-Stokes equations are reorganized in the wave form, which reduces the overall sound problem to a more simplified wave equation associated with a source term. The far-field pressure is defined in terms of an integral over the volume or the surface that contains the sources.

The first integral approach in predicting acoustic propagation is the acoustic analogy. By taking the time derivative of the mass conservation law and subtracting the divergence of the momentum equation, a wave-type equation is obtained. The difference between the actual flow and the reference flow is identified as a source of sound. This idea was introduced by Lighthill (Michael J Lighthill 1952), who called this an analogy. The second key in Lighthill's idea is the use of integral equations as a formal solution,

such that acoustic field is obtained as a convolution of the Green's function and the sound source.

The theory is based on the equations of motion of a gas, for the purpose of estimating the sound radiated from a fluid flow as a result of instability, containing regular fluctuations or turbulence (Michael James Lighthill 1954). Some questions have been raised to the initial formulation, for example Lilley (Lilley 1974), as to which terms should be identified as source terms and which parts should be accounted for as wave operators of the equation. However, the main cause for concern with the acoustic analogy method is that it introduces a certain difficulty in accounting for refraction effects and shock noise, which are clearly of importance when dealing with supersonic flows (A. Lyrantzis 2003). Several extensions to the acoustic analogy have been proposed. For instance, Ffowcs Williams and Hawkings (Williams and Hawkings 1969) (FW-H) equations were proposed to extend the acoustic analogy in the case of solid surfaces which will be explained thoroughly in the following sections.

Kirchhoff Method

Another approach to predict the sound propagation is to assume that the sound transmission is governed by the simple wave equation. The original idea of matching the nonlinear aerodynamic near-field and linear acoustic far-field was first introduced by Hawkings (Hawkings 1979). The Kirchhoff method is also based on separation of the computation domain to nonlinear near-field which is usually calculated numerically and the linear far-field region which is evaluated by linear Kirchhoff formulation.

The far-field solution is evaluated on a control surface around nonlinear region which is assumed that encloses all the nonlinearities and sources. The sound pressure can

be calculated by an integration of the pressure on the control surface and its normal and time derivatives. This method is simple and accurate as long as all the nonlinearities and quadrupole sound sources are accounted for inside the surface and can be a better alternative to traditional acoustic analogy. George and Lyrintzis (George and Lyrintzis 1986) introduced the “Kirchhoff Method” terminology and applied the method for the first time (A. Lyrintzis 2003).

Kirchhoff Method has been used for various aero-acoustic applications. Farassat and Meyers (F Farassat and Myers 1988) derived Kirchhoff formulation for moving and deformable surfaces with partial derivatives which were easy enough to use in numerical computations. Farassat’s Kirchhoff formulation defines a far-field solution in terms of sources enclosed within the Kirchhoff surface as a solution to the linear, homogenous wave equation. The far-field signal is evaluated with a surface integral over a control surface of any acoustic variable (e.g. disturbance pressure), its normal derivatives, and time derivatives. The surface integrals over the control surface account for the retarded time (Myers and Hausmann 1990).

It is also possible to simplify Farassat’s formulation for stationary surfaces. By application of Fourier transformation the surface integral equation can be expressed in the frequency domain, which is basically expressing the solution as Helmholtz equations. Lyrintzis and Mankbadi (A S Lyrintzis and Mankbadi 1996) employed the three dimensional Kirchhoff formulation both in time domain and frequency domain in jet noise aeroacoustics application. Pilon (Pilon and Lyrintzis 1997) developed two dimensional formulations for Kirchhoff method. A complete review of several applications of Kirchhoff method in aeroacoustics is given by Lyrintzis (Anastasios S

Lyrintzis 1994).

One of the challenges in application of the original Kirchhoff methods has been calculation of normal derivatives of pressure on the control surface. Although, with today's advancements in computer processing, accurate numerical calculations of normal derivatives can be achieved faster, but implementing methods which do not require these numerical calculations is still an appealing factor. Mankbadi et al (R R Mankbadi et al. 1996) developed a modified Green's function for cylindrical control surface to predict the far-field noise propagation in jet noise application using Surface Integral Formulation (SIF) without the need for normal derivatives, extending the large scale nonlinear three dimensional source solution to linear far-field that is governed by wave equation or Helmholtz equation in frequency domain.

Atassi et al (H M Atassi, Dusey, and Davis 1993; Hafiz M Atassi, Subramaniam, and Scott 1990) developed a two dimensional formulation in frequency domain, employing a modified Green's function for a circular Kirchhoff surface to eliminate the need to evaluate the normal derivatives of pressure. In the work of Atassi and co-workers, the Green's function is expressed in terms of infinite series of higher order Hankel functions. Since the usual grid for the near-field solutions of airfoil noise problems is elliptic, the pressure Kirchhoff surface must be interpolated and then differentiated numerically.

Hariharan et al (Hariharan, Scott, and Kreider 2000) introduced a Potential-Theoretic Method (PTM) as a an alternative framework to classical Kirchhoff formulations in frequency domain, not requiring the normal derivatives on control surface. In addition, PTM relies on the use of arbitrary Kirchhoff surface, which makes

this method appealing and easier to implement (No interpolations are required to calculate the pressure on the Kirchhoff surface). The PTM formulation and framework employed will be discussed thoroughly in the following chapters, since it has been used for application of airfoil noise for this work.

Ffowcs Williams - Hawkings Method

Another alternative in acoustic predictions using surface integral methods is FW-H equations. The original philosophy is to assume the FW-H equation as integration over an impenetrable surface, the general equation can be derived if the surface is assumed to be porous as mentioned by Ffowcs Williams and Hawking (Williams and Hawkings 1969) originally. Similar to the Kirchhoff method the quantities on the porous control surface can be used to predict the far-field pressure signal. The FW-H equation is a rearrangement of the exact continuity and Navier-Stokes equations. A complete comparison of different formulations of the FW-H equations is given in the first reference (A. Lyrntzis 2003), also a review of all equations of FW-H and Kirchhoff for noise propagation of rotating blades application is given by Farassat (F Farassat 2001). Also, a thorough comparison between two methods is conducted by Pilon and Lyrntzis (Pilon (1997)).

In the FW-H approach, time histories of all flow variables are needed but no spatial derivatives of the variables are required. The far-field solution requires surface and volume integral but for most cases the volume integral can be approximated or neglected, since the volume integral evaluations might be hard to calculate. Singer et al (Singer et al. 2000) demonstrated that when control surface is located in the nonlinear region, the FW-H approach correctly filters out the part of the solution that does not

radiate as sound, while Kirchhoff gives incorrect results. In many applications of the FW-H equation in the area of rotorcraft aeroacoustics (Di Francescantonio 1997; Strawn and Biswas 1995), the method has been applied such that the control surface coincides with the surface of the solid body. However, the method is still applicable when the control surface is off the body and the surface is permeable.

Farassat's formulation (Feri Farassat 1981) for FW-H equation seems to be the optimal approach in three dimensional flows. Brentner and Farassat (Brentner and Farassat 1997) showed very good results for moving surfaces. Lyrintzis and Uzun (A S Lyrintzis and Uzun 2001) developed a FW-H approach for the noise prediction of three dimensional turbulent jet using stationary integration surface both in time domain and frequency domain. Lockard (Lockard 2002) evaluated the noise propagation airframe noise for subsonic, rectilinear surface using time and frequency domain formulations of FW-H equations.

In spite of the fact that most significant acoustic phenomena are three dimensional and such relevant formulations should be preferred, the computational cost of generating near-field data can often be restricting. In addition, the noise generating flow structures can be pseudo-two dimensional with the correlation length in third direction. In this case, two dimensional formulations should give correct features of the radiated sound but over-predict the amplitude. Two dimensional results should predict the radiated acoustic trends and give some fundamental information for three dimensional results such as required resolution. A comparison of two and three dimensional solutions for slat noise has been given by Singer et al (Singer, Lockard, and Brentner 2000) and it is demonstrated that two dimensional results are useful. Although two dimensional results do not capture the

entire physics of the problem, they can be used to acquire estimations of the acoustic sources that extend along the span. Lockard (Lockard 2000) presents a two dimensional formulation of the FW-H equations with its important properties that is robust and easy to implement, in order to extend the CFD solution to far-field acoustics. Lockard's (Lockard 2000) two dimensional formulation demonstrate very good results for the noise generated by the shedding of vorticity from a circular cylinder and these formulations are explained thoroughly in the following chapters, since the same formulation of FW-H method is used in this work.

2. Computational Fluid Dynamics of Near-Field

Several CFD approaches can be utilized, ranging from lower accuracy Reynolds-Averaged Navier–Stokes (RANS) to the higher accuracy Direct Numerical Simulations (DNS), with Detached-Eddy Simulations (DES) and Large-Eddy Simulations (LES) as compromises between accuracy and efficiency. In this chapter, the near-field Large Eddy Simulation (LES) test parameters, process, and results are presented in order to demonstrate a brief overview of the physical aspects of the study and to establish basis for the interpretations that will be made through extension of solution to far-field using the surface integral methods.

2.1. Computational Fluid Dynamics Formulation

In order to obtain the near-field solution of the noise generating transitional airfoil for this study, high-accuracy FDL3DI code has been employed by acknowledged colleagues at Embry-Riddle Aeronautical University CFD research group (Golubev et al.). The numerical code solves the compressible Navier-Stokes equations represented in strong conservative, time-dependent form in the generalized curvilinear computational coordinates (ξ, η, ζ, τ) transformed from the physical coordinates (x, y, z, t) :

$$\frac{\partial}{\partial \tau} \left(\frac{\vec{Q}}{J} \right) + \frac{\partial \vec{F}_i}{\partial \xi} + \frac{\partial \vec{G}_i}{\partial \eta} + \frac{\partial \vec{H}_i}{\partial \zeta} + \frac{1}{\text{Re}} \left[\frac{\partial \vec{F}_v}{\partial \xi} + \frac{\partial \vec{G}_v}{\partial \eta} + \frac{\partial \vec{H}_v}{\partial \zeta} \right] = \vec{S} \quad (2.1)$$

The solution vector $\vec{Q} = (\rho, \rho u, \rho v, \rho w, \rho e)$ is defined in terms of the flow density ρ , Cartesian flow velocity components (u, v, w) , and flow specific energy,

$$e = \frac{T}{\gamma(\gamma-1)M_\infty^2} + \frac{1}{2}(u^2 + v^2 + w^2), \quad (2.2)$$

with the assumption of perfect gas relationship $p = \rho T / \gamma M_\infty^2$ connecting the flow pressure p , temperature T , and the freestream Mach number M_∞ (γ is the specific heat ratio). The other variables in Eq. (2.1) include the inviscid flux vectors defined by,

$$\vec{F}_i = \begin{bmatrix} \rho \hat{u} \\ \rho u \hat{u} + \hat{\xi}_x p \\ \rho v \hat{u} + \hat{\xi}_y p \\ \rho w \hat{u} + \hat{\xi}_z p \\ (\rho e + p) \hat{u} - \hat{\xi}_t p \end{bmatrix}, \quad \vec{G}_i = \begin{bmatrix} \rho \hat{v} \\ \rho u \hat{v} + \hat{\eta}_x p \\ \rho v \hat{v} + \hat{\eta}_y p \\ \rho w \hat{v} + \hat{\eta}_z p \\ (\rho e + p) \hat{v} - \hat{\eta}_t p \end{bmatrix}, \quad \vec{H}_i = \begin{bmatrix} \rho \hat{w} \\ \rho u \hat{w} + \hat{\zeta}_x p \\ \rho v \hat{w} + \hat{\zeta}_y p \\ \rho w \hat{w} + \hat{\zeta}_z p \\ (\rho e + p) \hat{w} - \hat{\zeta}_t p \end{bmatrix}, \quad (2.3)$$

the transformation Jacobian, $J = \partial(\xi, \eta, \zeta, \tau) / \partial(x, y, z, t)$, the metric quantities defined,

e.g., as $\hat{\xi}_x = (J^{-1}) \partial \xi / \partial x$, etc., and the transformed flow velocity components,

$$\begin{aligned} \hat{u} &= \hat{\xi}_t + \hat{\xi}_x u + \hat{\xi}_y v + \hat{\xi}_z w \\ \hat{v} &= \hat{\eta}_t + \hat{\eta}_x u + \hat{\eta}_y v + \hat{\eta}_z w \\ \hat{w} &= \hat{\zeta}_t + \hat{\zeta}_x u + \hat{\zeta}_y v + \hat{\zeta}_z w \end{aligned} \quad (2.4)$$

The viscous flux vectors, \vec{F}_v , \vec{G}_v and \vec{H}_v , are defined, e.g., (Pletcher, Tannehill, and Anderson 2012) while \vec{S} represents the source term which allows incompressible unsteady vortical perturbation to be introduced into the flow field. All flow variables are normalized by their respective reference freestream values except for pressure which is non-dimensionalized by $\rho_\infty u_\infty^2$.

The governing equations are represented in the original unfiltered form used

unchanged in laminar, transitional or fully turbulent regions of the flow. Visbal et al (Visbal, Morgan, and Rizzetta 2003) provide further details on the code's employed ILES procedure in which a high-order low-pass filter operator is applied to the dependent variables during the solution process. The resulting filter selectively damps the evolving poorly resolved high-frequency content of the solution.

The code employs a finite-difference approach to discretize the governing equations, with all the spatial derivatives obtained using the high-order compact-differencing schemes (Lele 1992). For the wing section computations of the current work, a 6th-order scheme is used. At boundary points, higher-order one-sided formulas are utilized which retain the tridiagonal form of the scheme and the time marching is accomplished by incorporating a 2nd-order iterative, implicit approximately-factored procedure as described.

2.2. The Acoustic Field Computation

In the previous numerical 2D studies by Golubev et al (Golubev et al. 2014), a 1281×789 O-mesh employed that was generated about NACA-0012 airfoil and efficiently partitioned into sets of overlapped blocks assigned to different processors during parallel implementations. As illustrated in Figure 2.1, the mesh is carefully clustered near the airfoil surface to achieve the wall-normal and wall-tangent mesh sizes of $\Delta y/c = 2.5 \times 10^{-5}$ and $\Delta x/c = 0.5 \times 10^{-3}$. In terms of the wall units $y_w^+/c = 3.13 \times 10^{-5}$ estimated for the characteristic flow condition with Mach number, $M = 0.0465$ and Reynolds number, $Re_c = 1.4 \times 10^5$, such grid refinement corresponds to the non-dimensional values of $\Delta y^+ \approx 1$ and $\Delta x^+ = 20$, with 12 grid points clustered in the region $0 < y^+ < 10$.

For the matter of completeness the three dimensional studies has been conducted

to generate the near-field data, so that pseudo-two dimensional studies can be carried out using the integral equations. For 3D simulations, such grid parameters correspond to a high-resolution LES that is even finer compared to the mesh employed in a similar DNS study by Desquesnes et al (Desquesnes, Terracol, and Sagaut 2007).

It should be noted that the use of 2D analysis in the preliminary studies was based on the assumption that though inherently unsteady, the investigated flow regimes remain primarily laminar (with possible separation zones) and exhibit transitional features. The current 3D ILES analysis employs a wing section with span-wise extension of $0.1c$, with periodic conditions applied at the span tip planes. Tables 1, shows the 2D and 3D grid configuration of the case studies.

Cases	Dimension	$\Delta y/c$	$\Delta x/c$
2D FINE	$1281 \times 789 \times 3$	2.5×10^{-5}	0.5×10^{-3}
3D FINE	$1281 \times 789 \times 101$	2.5×10^{-5}	0.5×10^{-3}

Table 2.1 NACA-0012 Grids employed in 2D and 3D studies.

The baseline 2D set-up employs a physical time step of 0.675×10^{-6} seconds (corresponding to dimensional time) whereas the 3D simulations require a much smaller time step of 0.16875×10^{-6} sec or 0.0225×10^{-5} non-dimensionalized time due to the fine grid spacing along the span. In all simulations, the steady-state flow conditions were first reached after marching for 20 characteristic cycles to remove all transient processes. The flow variable signals were then recorded for over 720,000 steps, hence for the baseline set-up collecting the data sample for 0.487 sec with the sampling rate of 33.6 kHz achieving the frequency resolution of $\Delta f = 2.05 \text{ Hz}$.

Since the integral solutions require flow variables as inputs for far-field evaluations, the flow variables on specific surfaces have been extracted and recorded. The PTM method requires pressure signal on the control surfaces and the FW-H approach requires all flow variables on the surface. Both of the surface integral approaches employed for this study are compatible with arbitrary shape for control surfaces. However, ellipse type control surface seems to be a reasonable choice for airfoil noise prediction problems. Such surface shapes are used by Hariharan et al (Hariharan, Scott, and Kreider 2000). Figure 2.1 shows the computational O-grid around NACA-0012 airfoil and the desired control surfaces around it to capture the data that can be used for the surface integral approaches.

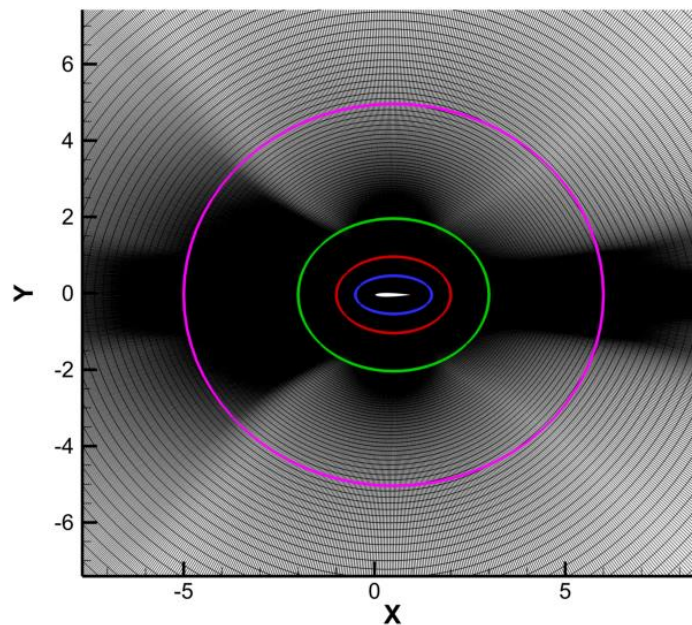


Figure 2.1 NACA-0012, Computational grid.

Furthermore, one of the advantages of using O-grids is that in order to obtain data on the desired control surfaces around the airfoil, data can be extracted easily by choosing certain grid indices curvilinear to the surface of airfoil, as illustrated in Figure 2.2.

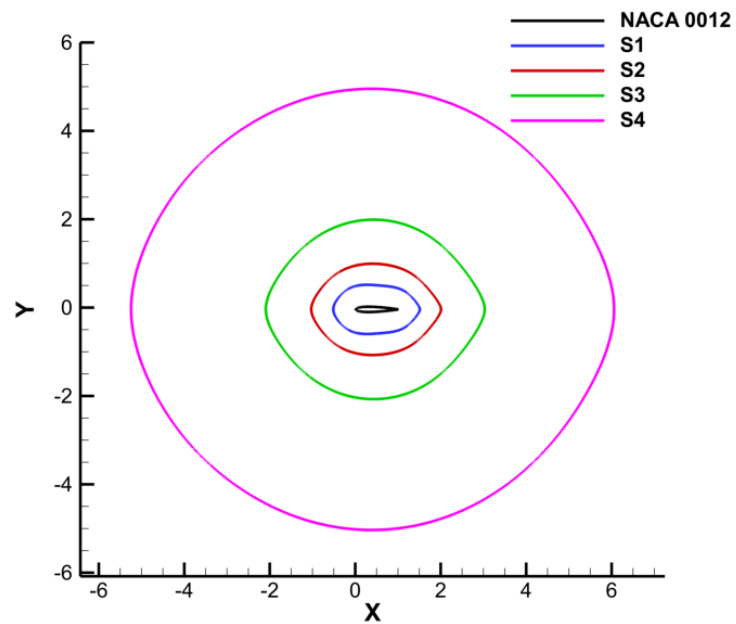


Figure 2.2 NACA-0012, Integration surfaces.

3. Surface Integral Methods Formulations

3.1. Surface Integral Formulations

The problem of noise in flow-acoustic resonant interactions in transitional airfoils in this work, can be addressed in two general categories. One, the nonlinear processes of noise generation due to resonant interactions in transitional airfoils, which is governed by the full, time-dependent compressible Navier-Stokes equations. Second, linear acoustic radiation of the generated source to far-field, which is evaluated employing surface integral methods. Following the original philosophy of aeroacoustics, one can consider two separate and distinct characteristics of the sound. The characteristics are the nonlinear generation of the sound, and then the linear propagation thereof. The linear characteristic of sound propagation allows to predict the acoustic radiation using integral methods such as FW-H and PTM approaches for this work.

3.2. Potential-Theoretic Method (PTM) Formulation

The method presented here, which is presented by Hariharan et al (Hariharan, Scott, and Kreider 2000), follows the philosophy of using Kirchhoff approach and constructing a modified Green's function to predict the far-field eliminating the need to require normal derivatives of pressure on the control surface, such as what was introduced by Atassi et al (H M Atassi, Dusey, and Davis 1993; Hafiz M Atassi, Subramaniam, and Scott 1990).

The PTM method presented here, as an advancement to previous formulations, has two goals. One, to simplify the computations of Green's function, and two, to allow a convex arbitrary shape for the Kirchhoff surface. It only requires free space Green's

function and an unknown density function. The single-layer density is determined by a technique proposed by Hariharan and MacCamy (Hariharan and MacCamy 1986) for electromagnetic scattering problems. Additionally, this method allows the use of any arbitrary shaped function that can be written in polar coordinates. This definitely increases the flexibility of the numerical implementation. This means that the Kirchhoff surface may be adjusted to match just about any numerical grid that may be used to determine the near-field pressure. As a result, interpolation of the pressure can be eliminated (as compared to Atassi's Formulation). The extension to three dimensional geometries can be obtained rigorously, but numerical procedures based on this method for two dimensional airfoil-gust interaction noise problems has been validated (Hariharan, Scott, and Kreider 2000).

3.2.1. Solution Formulation

As shown in Figure 3.1, a Kirchhoff surface Γ , is considered around the airfoil in the near-field which is assumed to be smooth, and is far enough from the solid surface so that the mean flow quantities in the region exterior to Kirchhoff surface, Ω , are only slightly different from free stream quantities. This allows the linearization of the continuity and momentum equations.

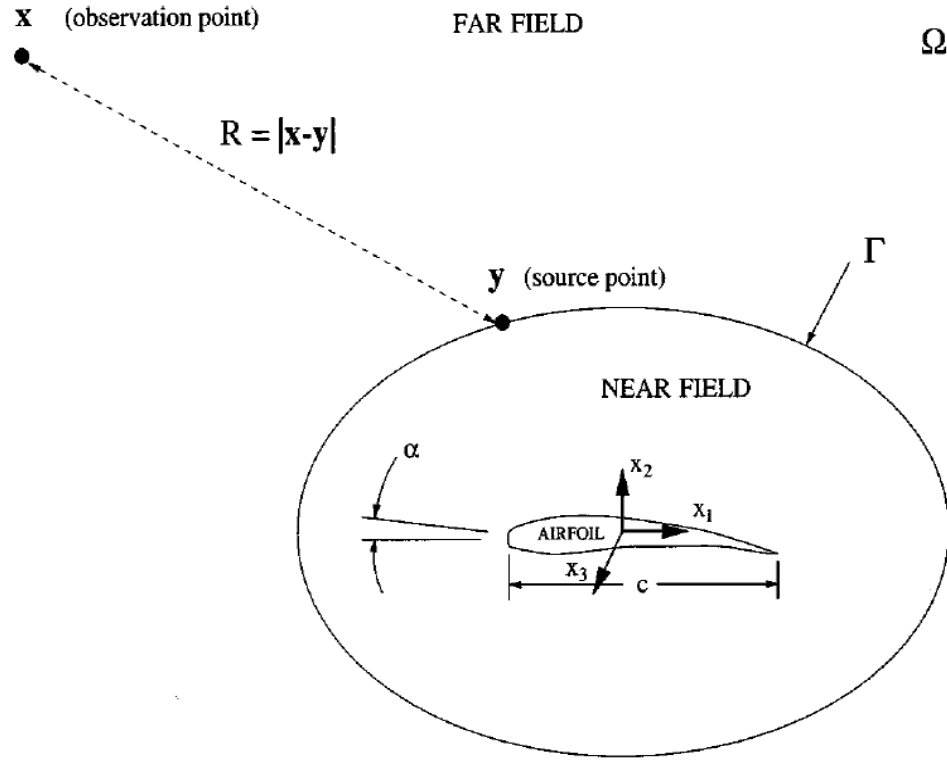


Figure 3.1 Problem configuration, Kirchhoff Surface around solid surface, (Hariharan et al (Hariharan, Scott, and Kreider 2000))

The coordinate system is transformed to the Prandtl-Glauert plane such as, $\tilde{x}_1 = x_1$ and $\tilde{x}_2 = \beta_\infty x_2$. Employing the linearization of continuity and momentum equation along with transforming the problem to the frequency domain, the problem reduced to classical exterior problem by Helmholtz equation with boundary conditions are calculated numerically using CFD.

$$\tilde{\nabla}^2 \bar{p} + K^2 \bar{p} = 0 \quad (3.1)$$

where Helmholtz number is $K = \frac{kM_\infty}{\beta_\infty^2}$, and wave number is $k = \frac{\omega}{c}$.

3.2.2. Solution Procedure

The pressure solution may be expressed as an integral equation in terms of the Green's function and the source term (unknown density function), as follows:

$$\bar{p}(\tilde{x}) = \int_{\tilde{\Gamma}} \sigma(\tilde{y}) G_f(\tilde{x} | \tilde{y}) ds_{\tilde{y}}, \quad \tilde{x} \in \tilde{\Omega}, \tilde{y} \in \tilde{\Gamma} \quad (3.2)$$

Where σ is the density function, G_f is the free-space Green's function

$$G_f(\tilde{x} | \tilde{y}) = -\frac{i}{4} H_0^{(1)}(K |\tilde{x} - \tilde{y}|), \quad (3.3)$$

And \bar{p} satisfies

- $\bar{p} \sim e^{iKR} / \sqrt{R}$ as $|\tilde{x}| \rightarrow \infty$ with $R = |\tilde{x} - \tilde{y}|$
- $\bar{p} = \tilde{f}(\tilde{x})$ on $\tilde{\Gamma}$

As \tilde{x} approaches the surface $\tilde{\Gamma}$, (3.2) becomes

$$\int_{\tilde{\Gamma}} \sigma(\tilde{y}) G_f(\tilde{x} | \tilde{y}) ds_{\tilde{y}} = \tilde{f}(\tilde{x}), \quad \tilde{x}, \tilde{y} \in \tilde{\Gamma} \quad (3.4)$$

The equation above is a single integral equation at a logarithmic singularity of the first kind. Several authors have shown that there exist various solutions to this type of equation. Some of the first results were presented by Hsiao and MacCamy (Hsiao and MacCamy 1973). A particular method for solving Eq. (3.4) for σ is shown in detail below. After having calculated σ and substituting in (3.2), one is then able to determine \bar{p} at any point $\tilde{x} \in \tilde{\Omega}$.

In order to allow the Kirchhoff surface to have an arbitrary shape, it should be assumed that $\tilde{\Gamma}$ is polar-representable. In other words, $\tilde{\Gamma}$ can be expressed as a function

$$r = R(\theta).$$

Let \tilde{x} and \tilde{y} (both located on $\tilde{\Gamma}$) be expressed in polar coordinates as:

$$\tilde{x}(\theta) = (R(\theta) \cos \theta, R(\theta) \sin \theta) \quad (3.5)$$

$$\tilde{y}(\phi) = (R(\phi) \cos \phi, R(\phi) \sin \phi), \quad (3.6)$$

And then assume that

$$\tilde{f}(\tilde{x}) \equiv \hat{f}(\theta), \quad \sigma(\tilde{y}) \equiv \hat{\sigma}(\phi) \quad (3.7)$$

The distance between the two points can then be calculated as such:

$$\begin{aligned} |\tilde{x} - \tilde{y}| &= \sqrt{R^2(\theta) + R^2(\phi) - 2R(\theta)R(\phi)\cos(\theta - \phi)} \\ &\equiv d(\theta, \phi), \end{aligned} \quad (3.8)$$

And the Green's function is then,

$$\begin{aligned} G_f(\tilde{x} | \tilde{y}) &= -\frac{i}{4} H_0^{(1)}(K |\tilde{x} - \tilde{y}|) \\ &= -\frac{i}{4} H_0^{(1)}(K \cdot d(\theta, \phi)) \\ &= \hat{G}(\theta | \phi). \end{aligned} \quad (3.9)$$

Then ds in terms of $d\phi$ is as follows:

$$ds = \sqrt{R'^2(\phi) + R^2(\phi)} d\phi. \quad (3.10)$$

If one substitutes these into (3.4):

$$\hat{f}(\theta) = \int_0^{2\pi} \hat{\sigma}(\phi) \hat{G}(\theta | \phi) \sqrt{R'^2(\phi) + R^2(\phi)} d\phi, \quad \theta \in [0, 2\pi). \quad (3.11)$$

Defining $\bar{\sigma}(\phi) \equiv \sigma(\phi) \sqrt{R'^2 + R^2}$, the final equation can be achieved as:

$$\hat{f}(\theta) = \int_0^{2\pi} \bar{\sigma}(\phi) \hat{G}(\theta | \phi) d\phi, \quad \theta \in [0, 2\pi). \quad (3.12)$$

There is a logarithmic singularity in \hat{G} (3.3) which makes a direct numerical approximation of (3.12) possible when $\theta = \phi$. Therefore the formulation must be rearranged such that it avoids numerical difficulties. In order to achieve that, first it should be noted that the Hankel function of the first kind may be expressed as such:

$$-\frac{i}{4} H_0^{(1)}(z) = \frac{1}{2\pi} \log(z) + \hat{\gamma} - \frac{i}{4} + \hat{T}(z), \quad (3.13)$$

where $\hat{\gamma} = (\gamma - \log(2)) / 2\pi$

In this case, γ is Euler's constant and $\hat{T}(z) \rightarrow 0$ as $z \rightarrow 0$. This is to say that \hat{G} can be represented as:

$$\hat{G}(\theta | \phi) = \frac{1}{2\pi} \log(K \cdot d(\theta, \phi)) + \hat{\gamma} - \frac{i}{4} + \hat{T}(K \cdot d(\theta, \phi)). \quad (3.14)$$

Then it is clear that, when $\theta \rightarrow \phi$, $R(\theta)$ can be expanded in a neighborhood of ϕ by using a Taylor series. This allows $d(\theta, \phi)$ to be written in the following limiting case as:

$$d(\theta, \phi) = 2 \sin\left(\frac{|\theta - \phi|}{2}\right) \sqrt{R'^2(\phi) + R^2(\phi)}. \quad (3.15)$$

This confines the singularity which arises in (3.13) to the factor $\log(\sin(|\theta - \phi|/2))$.

Rewriting (3.11):

$$\hat{f}(\theta) = \int_0^{2\pi} (\bar{\sigma}(\phi) - \bar{\sigma}(\theta)) \hat{G}(\theta | \phi) d\phi + \bar{\sigma}(\theta) + \int_0^{2\pi} \hat{G}(\theta | \phi) d\phi, \quad \theta \in [0, 2\pi). \quad (3.16)$$

The formulation written above is much more favorable than (3.12) for two reasons. First, as one may notice, the first integral in (3.16) can be easily computed numerically because

the integrand can be shown to approach zero as $\theta \rightarrow \phi$. Second, the singularity in \hat{G} that appears in the second integral can be drawn out analytically, which leaves an integral with a regular integrand which also can be computed numerically without any difficulty. Substituting (3.14) and (3.15) into \hat{G} yields the expression for the second integral, for $\theta \in [0, 2\pi)$,

$$\begin{aligned} \int_0^{2\pi} \hat{G}(\theta | \phi) d\phi &= \int_0^{2\pi} \left[\frac{1}{2\pi} \log(Q) + \hat{\gamma} - \frac{1}{4} + \hat{T}(\theta, \phi) \right] d\phi \\ &= \int_0^{2\pi} \frac{1}{2\pi} \left[\log \left(\sin \left(\frac{|\theta - \phi|}{2} \right) \right) + \bar{T}(\theta, \phi) \right] d\phi, \end{aligned} \quad (3.17)$$

where \bar{T} and Q are defined as:

$$\bar{T} = \begin{cases} \hat{\gamma} - \frac{i}{4} + \frac{1}{2\pi} \log(2K \sqrt{R'^2(\phi) + R^2(\phi)}), & \theta = \phi \\ -\frac{1}{4} H_0^{(1)}(K \cdot d(\theta, \phi)) - \frac{1}{2\pi} \log \left(\sin \left[\frac{|\theta - \phi|}{2} \right] \right), & \theta \neq \phi \end{cases} \quad (3.18)$$

$$Q = 2K \sqrt{R'^2(\phi) + R^2(\phi)} \sin \left(\frac{|\theta - \phi|}{2} \right). \quad (3.19)$$

Since \bar{T} is regular and the singularity appears only in the first term on the right in (3.17).

Using complex analysis, specifically the value of the integral can be obtained as:

$$\frac{1}{2\pi} \int_0^{2\pi} \log \left(\sin \left(\frac{|\theta - \phi|}{2} \right) \right) d\phi = -\log(2). \quad (3.20)$$

substituting into (3.16), we get:

$$\hat{f}(\theta) = \int_0^{2\pi} (\bar{\sigma}(\phi) - \bar{\sigma}(\theta)) \hat{G}(\theta | \phi) d\phi - \bar{\sigma}(\theta) \log(2) + \bar{\sigma}(\theta) \int_0^{2\pi} \bar{T}(\theta, \phi) d\phi, \quad \theta \in [0, 2\pi) \quad (3.21)$$

This final form of the equation can easily be computed numerically because the two integrands are regular. The numerical procedure for finding $\bar{\sigma}$ can be developed easily.

3.2.3. Numerical Procedure

In order to evaluate the far-field solution numerically, a suitable shape for the Kirchhoff surface must be specified. The choice of an ellipse is convenient, not only because analytical representations for $R(\theta)$ and $R'(\theta)$ are available, but also because it is most convenient to solve for the near-field pressure using elliptic coordinates, so that the Kirchhoff surface may be specified on a near-field gridline to avoid interpolation error for the pressure (Hariharan, Scott, and Kreider 2000). To evaluate the far-field pressure, (3.21) should be solved numerically so it can be used in (3.2). The Numerical procedure is described below.

A numerical representation of (3.21) can be found using rectangular quadrature.

One can choose a discretization constant n and assume that, $h = 2\pi / n$.

For $i, j = 1, \dots, n$, define $\phi_j = (j - 1/2)h$ and $\theta_i = (i - 1/2)h$. Then, (3.21) becomes:

$$\sum_{j=1}^n A_{ij} \bar{\sigma}_j = \hat{f}_i \quad (3.22)$$

Where $A_{ij} = A(\theta_i, \phi_j)$, $\bar{\sigma}_j = \bar{\sigma}(\phi_j)$, and $\hat{f}_i = \hat{f}(\theta_i)$. The near-field solver is used to determine the values of \bar{p} , and hence \hat{f}_i , at a finite number of points on the Kirchhoff surface. The A_{ij} values are defined as such:

$$A_{ij} = \begin{cases} -\log(2) + \left[\sum_{k=1}^n \bar{T}_{ik} h - \sum_{k=1, (k \neq i)}^n \hat{G}_{ik} h \right], & i = j \\ \hat{G}_{ik} h, & i \neq j \end{cases}, \quad (3.23)$$

Where $\bar{T}_{ij} = \bar{T}(\theta_i, \phi_j)$ and $\hat{G}_{ij} = \hat{G}(\theta_i, \phi_j)$. An equation is obtained for each $i = 1, \dots, n$, yielding a $n \times n$ linear system, which can be solved by any standard method for the unknowns $\bar{\sigma}_1, \dots, \bar{\sigma}_n$.

Once $\{\bar{\sigma}_j\}$ is found, it is easy to find \bar{p} at any point $x \in \Omega$.

It is necessary to transform the point to $\tilde{x} \in \tilde{\Omega}$ using the Prandtl-Gauert plane translation.

Let \tilde{x} be represented as:

$$\tilde{x} = (r \cos \theta, r \sin \theta) \quad (3.24)$$

Where r and θ are fixed, and let $\tilde{y} \in \tilde{\Gamma}$ be defined as

$$\tilde{y} = (R(\phi) \cos \phi, R(\phi) \sin \phi), \quad \phi \in [0, 2\pi) \quad (3.25)$$

Therefore, the distance between \tilde{x} and \tilde{y} is defined by:

$$|\tilde{x} - \tilde{y}| = \sqrt{[r \cos \theta - R(\phi) \cos \phi]^2 + [r \sin \theta - R(\phi) \sin \phi]^2} \quad (3.26)$$

$$\begin{aligned} |\tilde{x} - \tilde{y}| &= \sqrt{[r^2 + R^2(\phi) - 2rR(\phi) \cos(\theta - \phi)]} \\ &= d(r, \theta, \phi), \end{aligned} \quad (3.27)$$

Consequently, the Green's function becomes:

$$\hat{G}(\theta, \phi) = -\frac{i}{4} H_0^{(1)}(K \cdot d(r, \theta, \phi)) \quad (3.28)$$

As follows from (3.2), the solution is:

$$\bar{p}(r, \theta) = -\frac{i}{4} \int_0^{2\pi} \bar{\sigma}(\phi) H_0^{(1)}(K \cdot d(r, \theta, \phi)) d\phi \quad (3.29)$$

This can be expressed numerically as:

$$\bar{p}(r, \theta) = -\frac{i}{4} \sum_{j=1}^n \bar{\sigma}_j H_0^{(1)}(K \cdot d(r, \theta, \phi)) \cdot h \quad (3.30)$$

3.3. Ffowcs Williams – Hawkings (FW-H) Formulation

Following the formulation presented by Lockard (Lockard 2000), the FW-H approach employed for this study is appropriate for two dimensional problems, robust, easy to implement, and has the important properties of FW-H method.

The FW-H equation in differential form as presented by Crighton et al (Crighton et al. 2012), can be expressed as:

$$\left(\frac{\partial^2}{\partial t^2} - c_0^2 \frac{\partial^2}{\partial x_i \partial x_i} \right) (H(f) \rho') = \frac{\partial^2}{\partial x_i \partial x_i} (T_{ij} H(f)) - \frac{\partial}{\partial x_i} (F_i \delta(f)) + \frac{\partial}{\partial t} (Q \delta(f)) \quad (3.31)$$

where

$$T_{ij} = \rho u_i u_j + P_{ij} - c_0^2 \rho' \delta_{ij} \quad (3.32)$$

$$F_i = (P_{ij} + \rho u_i (u_j - v_j)) \frac{\partial f}{\partial x_i} \quad (3.33)$$

$$Q_i = (p_0 v_i + \rho (u_i - v_i)) \frac{\partial f}{\partial x_i} \quad (3.34)$$

The contribution of the Lighthill's stress tensor, T_{ij} , to the right hand side of the FW-H equation is known as the quadrupole term. The dipole term, F_i , relates to an

unsteady force, Q , involves the monopole contribution that can be considered as an unsteady mass addition.

As illustrated in figure 3.1, $f = 0$ represents the control surface where the far-field solution is to be instigated. The Heaviside function, $H(f)$, is unity for $f > 0$ and zero for $f < 0$. The derivative of the Heaviside function is Dirac delta function ($H'(f) = \delta(f)$), which means zero for $f \neq 0$, but when integrated over a region including $f = 0$, the Dirac delta function yields a finite value

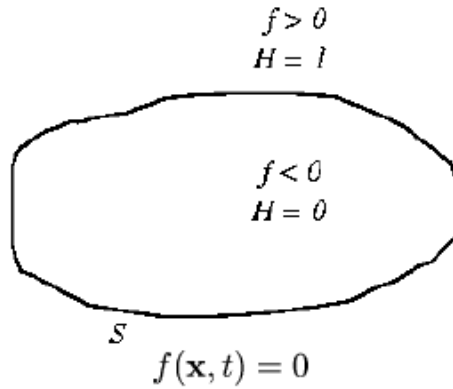


Figure 3.2 The surface assumed in the FW-H. (Kenneth S and Farassat 1997)

p and ρ , are the total pressure and density. u_i is fluid velocity, where as v_j is considered as the velocity of surface f . The Kronecker delta δ_{ij} , is unity for $i = j$, and zero otherwise. The prime represents the disturbance quantities relative to the free stream conditions defined by subscript "o". x_i , is the Cartesian coordinates and t stands for time. f can be prescribed as a function of time, so that it always surrounds a moving surface. The inviscid part of the compressive stress tensor, P_{ij} , is used ($P_{ij} = p\delta_{ij}$).

The time domain solution of the equation (3.31) can be presented by the Green's function for the wave equation,

$$\left(\frac{\partial^2}{\partial t^2} - c_0^2 \frac{\partial^2}{\partial x_i \partial x_i}\right) G(x, t; \xi, \tau) = \delta(x - \xi) \delta(t - \tau) \quad (3.35)$$

where ξ and t are the source coordinates and time respectively. The Green's function for such equation in two dimensions can be expressed as:

$$G(x, t; \xi, \tau) = \frac{H(c_o(t - \tau) - r)}{2\pi c_o \sqrt{c_0^2(t - \tau)^2 - r^2}} \quad (3.36)$$

where $r = |x - \xi|$. Now the solution of the equation (3.31) can be expressed as a convolution of Green's function and source terms on the right hand side of the FW-H equation, described as S .

$$H(f)\rho'(x, t) = \int_{-\infty}^{\infty} \int_{-\infty}^{\infty} S(\xi, \tau) \frac{H(c_o(t - \tau) - r)}{2\pi c_o \sqrt{c_0^2(t - \tau)^2 - r^2}} d\xi d\tau \quad (3.37)$$

where the infinite integral is over the entire two dimensional space. Using the Dirac delta function for monopole and dipole terms of $S(\xi, \tau)$, reduces the infinite in spatial integral to line integrals, however, the quadrupole term cannot be simplified. The surface can be located outside of all the regions where quadrupole term is significant. The major difficulty in calculation of equation (3.37) is the infinite time integral. The Heaviside function can change the upper limit, but the lower limit will always be infinite. In other words, an infinitely long time signal is required to account for all the contributions of sources throughout the third spatial dimension, as a result of tail effects in two dimensions. The three dimensional Green's function includes a delta function that can be employed to evaluate the time integral.

A simpler formulation can be achieved that does not approximate the two dimensional nature of the problem. To eliminate the inefficient time integration, the problem can be transformed to frequency domain. The direct Fourier transform to the original FW-H equation would not be useful because the shifting property of the $\delta(f)$ functions would be used in transform and would make it difficult to simplify the spatial integrals. However, a more appropriate form can be achieved by assuming a specific time dependence of the surface function. A useful assumption of uniform rectilinear motion, $f = f(x + Ut)$, can be made where the components of U , describe the motion of the surface. By application of the Galilean transformation from (x, t) to (t, \bar{t}) ,

$$y_i = x_i + U_i t, \quad \bar{t} = t \quad (3.38)$$

$$\frac{\partial}{\partial x_i} = \frac{\partial}{\partial y_i}, \quad \frac{\partial}{\partial t} = \frac{\partial}{\partial \bar{t}} + U_i \frac{\partial}{\partial y_i} \quad (3.39)$$

the equation (3.31) leads to

$$\begin{aligned} & \left(\frac{\partial^2}{\partial t^2} + U_i U_j \frac{\partial^2}{\partial y_i \partial y_j} + 2U_i \frac{\partial^2}{\partial y_i \partial \bar{t}} - c_0^2 \frac{\partial^2}{\partial y_i \partial y_i} \right) (H(f) \rho') \\ & = \frac{\partial^2}{\partial y_i \partial y_j} (T_{ij} H(f)) - \frac{\partial}{\partial y_i} (F_i \delta(f)) + \frac{\partial}{\partial \bar{t}} (Q \delta(f)) \end{aligned} \quad (3.40)$$

The term T_{ij} , remained unchanged and $f = f(y)$ is now only function of the spatial coordinates. The surface velocities, v_i , are replaced by $-U_i$. And the monopole and dipole terms are as:

$$F_i = (p \delta_{ij} + \rho(u_i - 2U_i) + \rho_0 U_i U_j) \frac{\partial f}{\partial y_j} \quad (3.41)$$

$$Q_i = (\rho u_i - \rho_0 U_i) \frac{\partial f}{\partial y_i} \quad (3.42)$$

The equation (3.40) is in a convenient formation to apply the Fourier analysis.

With the application of Fourier transform pair

$$\bar{F}\{q(t)\} = q(\omega) = \int_{-\infty}^{\infty} q(t) e^{-i\omega t} dt \quad (3.43)$$

$$\bar{F}^{-1}\{q(\omega)\} = q(w) = \frac{1}{2\pi} \int_{-\infty}^{\infty} q(\omega) e^{-i\omega t} dt \quad (3.44)$$

The final form of the FW-H equation in frequency domain becomes.

$$\begin{aligned} & \left(\frac{\partial^2}{\partial y_i \partial y_j} + k^2 - 2iM_i k \frac{\partial}{\partial y_i} - 2M_i M_j \frac{\partial^2}{\partial y_i \partial y_j} \right) (H(f) c_0^2 \rho'(y, \omega)) \\ &= \frac{\partial}{\partial y_i} (F_i(y, \omega) \delta(f)) - i\omega Q(y, \omega) \delta(f) \\ & - \frac{\partial^2}{\partial y_i \partial y_j} (T_{ij}(y, \omega) H(f)) \end{aligned} \quad (3.40)$$

Where wave number is $k = \omega/c_o$ and Mach number is $M = U/c_o$

It should be noted that the Fourier transform has been applied on the groupings T_{ij} , F_i , and Q , since the equation is linear in these terms. In the numerical applications the products are found first in time domain and then the Fast Fourier Transform (FFT) is applied on the FW-H variables.

Lockard (Lockard 2000; Lockard 2002) presents the Green's function for equation (3.40) for the subsonic flow regime ($M < 1$), obtained from Prandtl-Glauert

transformation. The ξ and η represent the two dimensional coordinates of the source, whereas the observer location is denoted by x and y .

$$G(x, y; \xi, \eta) = \frac{i}{4\beta} e^{\frac{iMk\bar{x}}{\beta^2}} H_0^2 \left(\frac{k}{\beta^2} \sqrt{\bar{x}^2 + \beta^2 \bar{y}^2} \right) \quad (3.41)$$

Where $\bar{x} = (x - \xi) \cos \theta + (y - \eta) \sin \theta$ and $\bar{y} = -(x - \xi) \sin \theta + (y - \eta) \cos \theta$. The angle θ is defined as $\tan \theta = U/V$ and $M = \frac{\sqrt{U^2 + V^2}}{c_o}$, H_0^2 is the Hankel function of the second kind of the order zero. And $\beta = \sqrt{1 - M^2}$ is the Prandtl-Glauert factor. By some mathematical manipulation (explained in the reference) (Lockard 2000) to the monopole, dipole and quadrupole terms of the integral solution of (3.40) the infinite integrals are transformed into integrals over the contour line defined by ($f = 0$).

The solution for equation (3.40) for ($M < 1$) can be expressed as:

$$\begin{aligned} H(f) c_0^2 \rho'(y, \omega) = & \\ & - \oint_{f=0} F_i(\xi, \omega) \frac{\partial G(y, \xi)}{\partial \xi_i} dl \\ & - \oint_{f=0} i\omega Q(\xi, \omega) G(y, \xi) dl \\ & - \int_{f>0} T_{ij}(\xi, \omega) H(f) \frac{\partial^2 G(y, \xi)}{\partial \xi_i \partial \xi_j} d\xi \end{aligned} \quad (3.42)$$

The Heaviside function illustrates that the solution at any point within the integration surface should be zero for all times. This is very good check for validation of accuracy of the computations.

For the purpose of application of the FW-H method to airfoil noise problem,

(following Lyrintzis and Uzun (A S Lyrintzis and Uzun 2001), Brentner and Farassat(Kenneth S and Farassat 1997), and Di Francescantonio (Di Francescantonio 1997)), the FW-H variables for the stationary surface and the case of formulation reduce to:

$$F_i = (p\delta_{ij} + \rho u_i u_j) \frac{\partial f}{\partial y_j} \quad (3.43)$$

$$Q_i = (\rho u_i) \frac{\partial f}{\partial y_i} \quad (3.44)$$

Equations (3.43) and (3.44) can be used only for the case of stationary monopole, since these sourcing terms do not include the convective velocity. Otherwise, the equations (3.41) and (3.42) are the most appropriate forms since they include the total velocities making them more appealing for the application to the CFD.

The quadrupole term has been neglected, because the calculation of the quadrupole is difficult to calculate due to its volume integral formulation and its calculation is complicated and numerically expensive. Moreover, as long as the integration surface is located outside the region where T_{ij} is large, the contribution of the quadrupole term is often small.

For the application of the FW-H equations into the numerical applications, the derivative of the Green's function have been calculated analytically. The monopole and dipole terms have been reduced to line integrals over the two dimensional surface ($f = 0$).

The entire solution process includes calculating the surface normal and forming

the F_i and Q terms using the time data on the integration surface, then performing FFT on the new variables, then evaluating the integral equation (3.42 formula without the volume integral term) to obtain the far-field acoustic pressure for each frequency and observer location.

4. Monopole Source Validation

Both PTM and FW-H formulations have been validated using a model problem. The first check is to evaluate the predicted signal when the observer point is located inside the surface and verify that solution goes to zero for the predicted noise. Both of the developed codes give zero values when the observer is positioned inside the surface.

Several model problems can be used to check the accuracy of each formulation. It should be noted that the desired model problem should be chosen properly. The addressed approaches in this study, are formulated such that to evaluate the radiated noise to far-field in two dimensional medium.

In order to validate the accuracy of FW-H and PTM codes developed for this study, a monopole source has been assumed to be located inside the Kirchhoff surface. The monopole source in two dimensional space can be prescribed as a line source that expands to infinity in the third dimension. The unsteady monopole source produces pressure fluctuations and behaves as an acoustic source. This approach is helpful since the analytical solution of the monopole source exists at any radius and the predicted sound pressure signal can be compared against the analytical solution. Another advantage of this study is that the sensitivity of the methods can be evaluated by changing parameters such as number of points on the control surface and the distance between the observer location and the surface.

The two dimensional monopole line noise source is located at the origin and the corresponding pressure and velocity equations are derived from the complex potential equation by Atassi (Hafiz M Atassi, Subramaniam, and Scott 1990) and Lockard (Lockard 2000) and Salomons (Salomons 2012), in terms of the Hankel function of the

second kind of order zero and one.

$$\phi(r, t) = A \frac{i}{4\beta} e^{i\left(\omega t + \frac{Mkx}{\beta^2}\right)} H_0^2\left(\frac{k}{\beta^2} r\right) \quad (4.1)$$

where $r = \sqrt{x^2 + \beta^2 y^2}$.

The variables needed for the PTM and FW-H are obtained from $p' = -\rho_0 \left(\frac{\partial \phi}{\partial t} + U_0 \frac{\partial \phi}{\partial x} \right)$, $u' = \nabla \phi$, and $\rho' = p'/c_0^2$. For the PTM method the pressure data is sufficient but the FW-H requires the velocities and the density. The pressure and velocity equations for the stationary monopole can be written as:

$$p(r, t) = -A \frac{i}{4} e^{i\omega t} H_0^2(kr) \quad (4.2)$$

$$\vec{u}(r, t) = -A \frac{i}{4} e^{i\omega t} H_1^2(kr) \frac{\vec{x} - \vec{y}}{r} \quad (4.3)$$

where r is the observer distance from the source and x and y represent the observer location and source coordinate in vector formation respectively.

Figure 4.1 illustrates the contours of the flow variables for the monopole acoustic source. Perturbation pressure and horizontal component of the perturbation velocity are shown on the top. The density contour structure is very similar to pressure and only levels are different because $\rho' = p'/c_0^2$. The horizontal and vertical components of the disturbed velocities are very similar.

For this case, the speed of sound is unity and all flow variables are non-dimensional. The control surface is a circle that is centered at the origin that has one unit radius. Fifty uniformly spaced points per wavelength are used on the integration surface. The observer point is located at $R = 10$.

Using the flow variables data on the source terms in the FW-H equations, Q and

F_i , are calculated and then FFT is applied on the source terms and finally the acoustic pressure is evaluated by employing the FW-H integral equation. Similarly for the PTM method, FFT of the pressure time history is calculated and used to calculate the density function source term in PTM formulation.

The figure 4.2 shows the Kirchhoff surface and observer location for an infinite monopole source line definition in two dimensions

After calculating the far-field signal the root mean square (RMS) of sound pressure signal has been calculated and compare with exact solution. Figure 4.3 and Figure 4.4 compare the predicted pressure RMS directivities from PTM and FW-H calculation with exact solution at the observer points at $R = 20$.

Also Figure 4.5, illustrates the comparison between stationary monopole case and the case that monopole is in flow of $M = 0.3$, for both methods. For this case, the speed of sound is unity and all variables are non-dimensional ($A = 0.01$, $\omega = 4\pi$). The control surface is a circle that is centered at the origin with radius of 5 unit length. Two hundred uniformly spaced points are used on the integration surface. The observer point is located at $R = 10$.

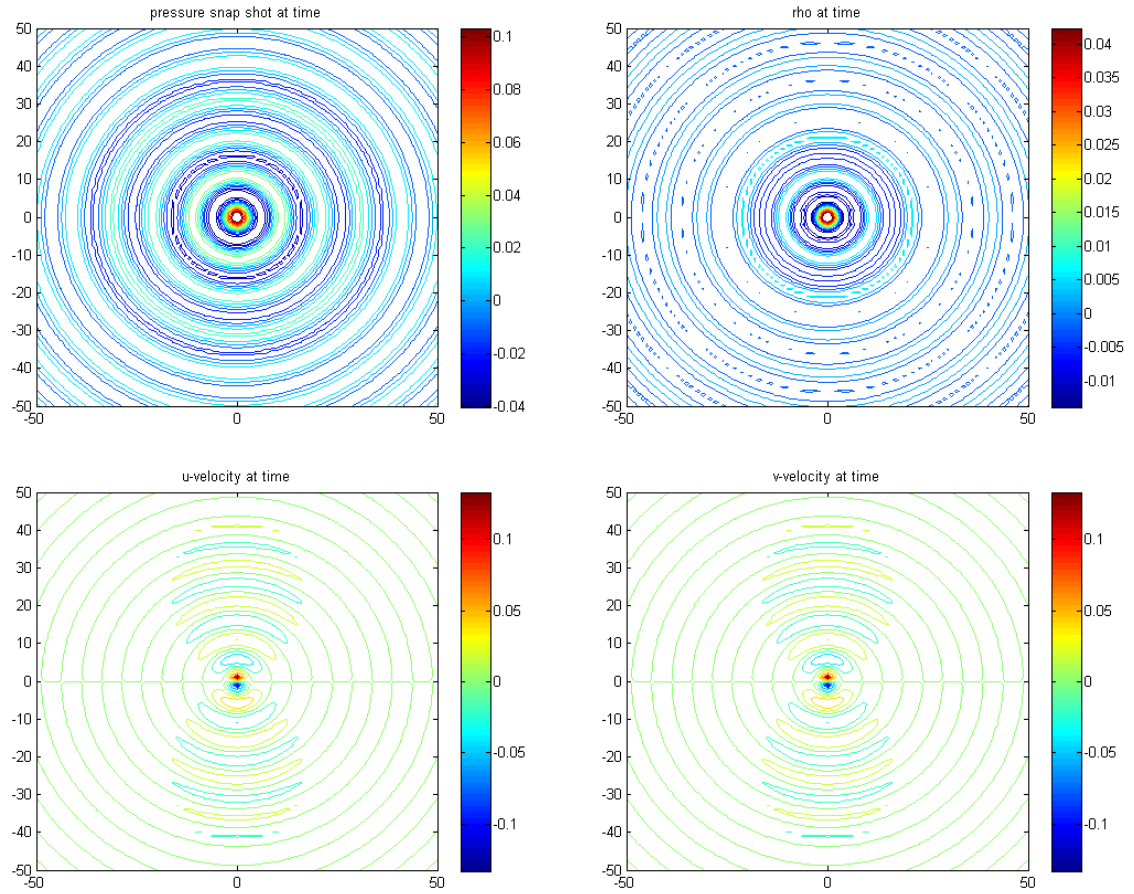


Figure 4.1 The perturbation flow variable contours of the monopole source term.

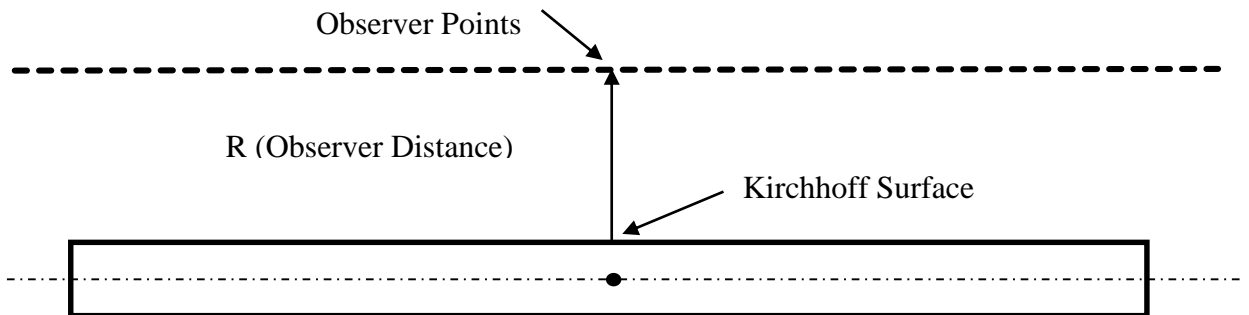


Figure 4.2 Monopole source, Kirchhoff surface, and Observer Location.

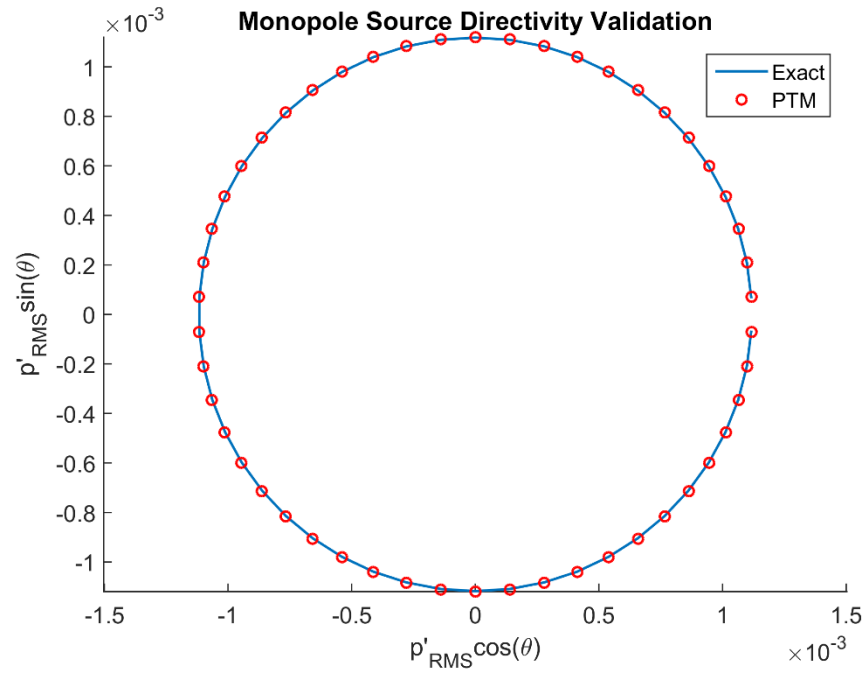


Figure 4.3 Directivity comparison of PTM at R=10 with exact solution for monopole source.

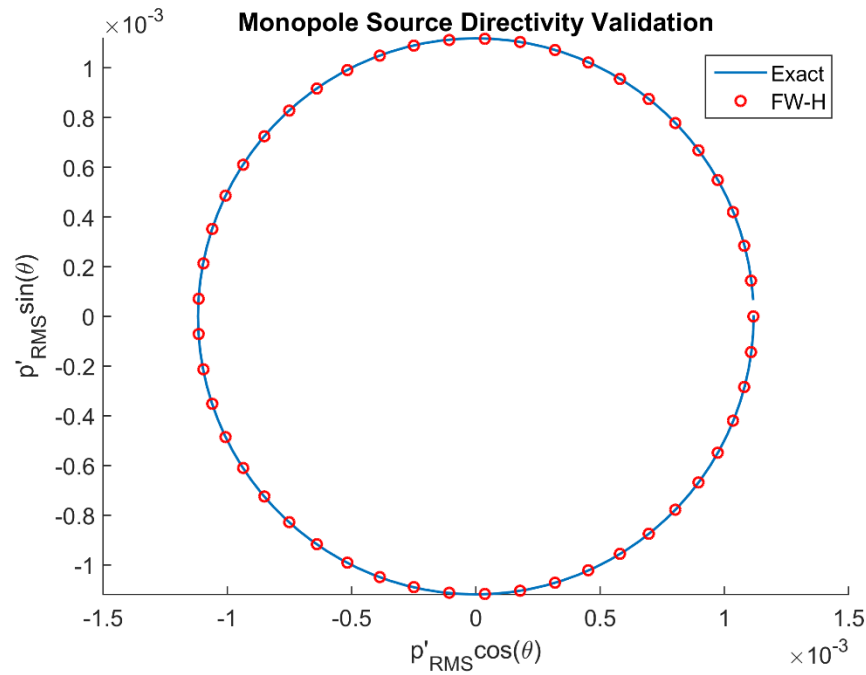


Figure 4.4 Directivity comparison of FW-H at R=10 with exact solution for monopole source.

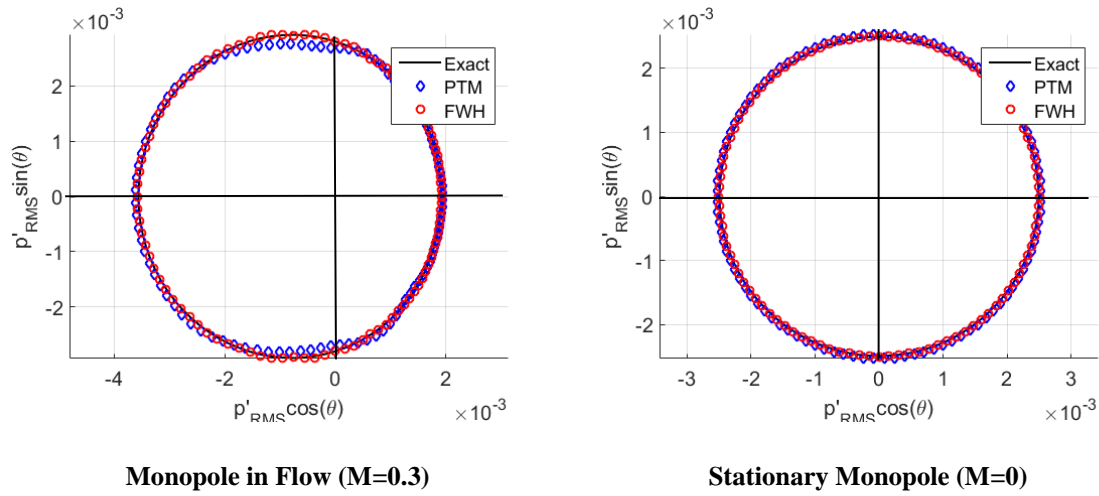


Figure 4.5 Acoustic pressure RMS directivity at $R=10$ of PTM (Blue) and FW-H (Magenta) with exact solution.

The agreement between predicted sound pressure and the exact solution is excellent in both methods, meaning that the formulations and developed codes for monopole source problems.

Now that predictions from both methods agree with the exact solution, the sensitivity of them can be investigated for variations of number of points on the integration surface and the distance of the observer location from Kirchhoff surface. For this sensitivity study, number of points on the control surface is fixed at $r = 1$ and the observer point is located at $R = 10$, for the stationary monopole case.

Figure 4.6 shows that by increasing the number of points per wavelength on the control surface, the RMS pressure error (relative to the exact solution) decreases. Although both behave similarly, but it is interesting to note that the FW-H method predicts the far-field sound pressure more accurately with the same number of points per wavelength than the PTM.

The other parameter that can be studied is the distance of the observer from the

control surface. This parameter has been evaluated as a ratio of the observer circle radius to Kirchhoff radius (R/r). For this study, fixed number of 15 points per wavelength has been used on the control surface at $r = 1$ and the observer distance has been varied from 1 to 10. Figure 3 indicates that, for small values of R/r the error of predicted far-field sound increases. The RMS error percentage difference between two methods has similar amount of as observed in Figure 4.6, since the number of points per wavelength is intentionally kept as 15. It is clear that both methods are unable to predict the far-field acoustics when the observer point is exactly on top of the control surface ($R = r$). It should also be noted that FW-H shows more accurate results than PTM when observer points is closer the Kirchhoff surface.

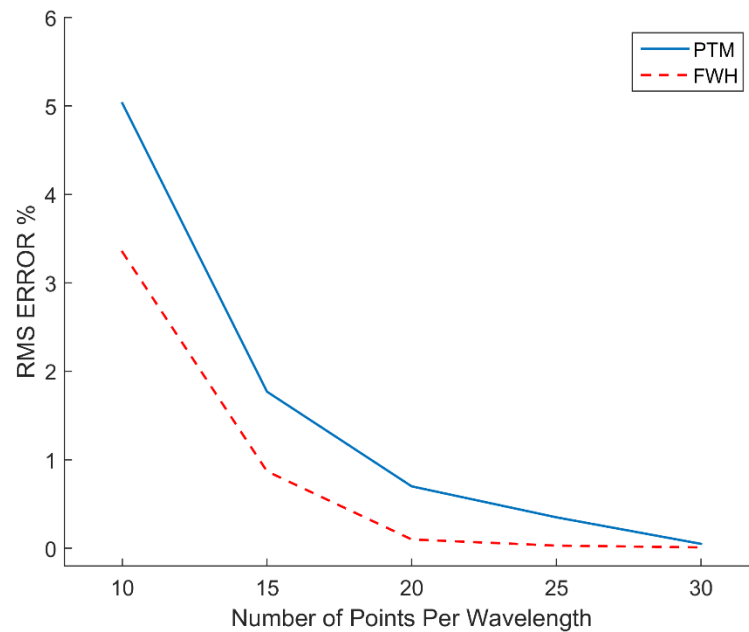


Figure 4.6 Error analysis: effect of number of points per wavelength on the surface.

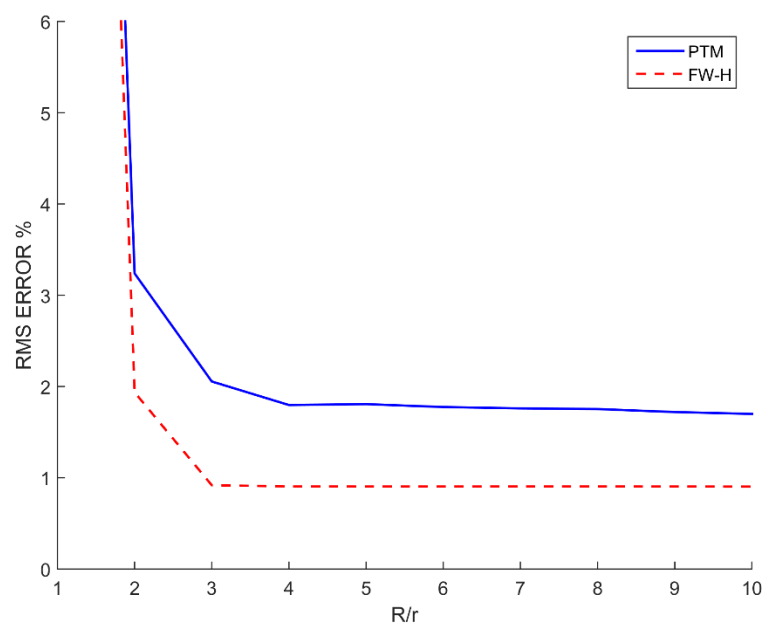


Figure 4.7 Error analysis: observer distance to control surface radius ratio (R/r).

5. Far-Field Acoustic Predictions of Transitional Airfoil Noise

The objective here is to employ the surface integral equation methods for the noise generating transitional airfoil problem. The noise generation of process of the problem in the near-field is highly nonlinear, so the high accuracy 2D simulations based on an Implicit Large Eddy Simulation (ILES) code are conducted for a NACA-0012 airfoil for varied conditions, to obtain the time-dependent flow variables in the near-field. Then the data is transferred to PTM and FW-H codes to evaluate the far-field noise acoustics. For the near-field high accuracy CFD simulations, a 1281x789 O-grid, selected based on the grid dependence study explained by Golubev et al (Golubev et al. 2013). The near-field data has been recorded in 0.26 seconds of dimensional physical time. The far-field acoustic results are predicted via the FW-H and PTM at 5 chords away to compare with direct results from CFD and also at 12.5 chords away to compare with the experimental data.

5.1. Near-Field results

A NACA-0012 airfoil with a chord $c = 0.12 \text{ m}$ at zero degree angle of attack is simulated in the transitional boundary condition with the free stream Mach number of 0.0465 and the Reynold number is $Re = 140,000$. Integration surfaces have been taken in elliptical shape surrounding the airfoil, using specific grid indices at different radial distance over chord ratios from airfoil surface. The control surfaces are located at $0.5c$, $1c$, $2c$, and $5c$ away from the airfoil surface. The Figure 5.1 shows an instantaneous vorticity field obtained from CFD calculation with the desired control surfaces super imposed on the contour.

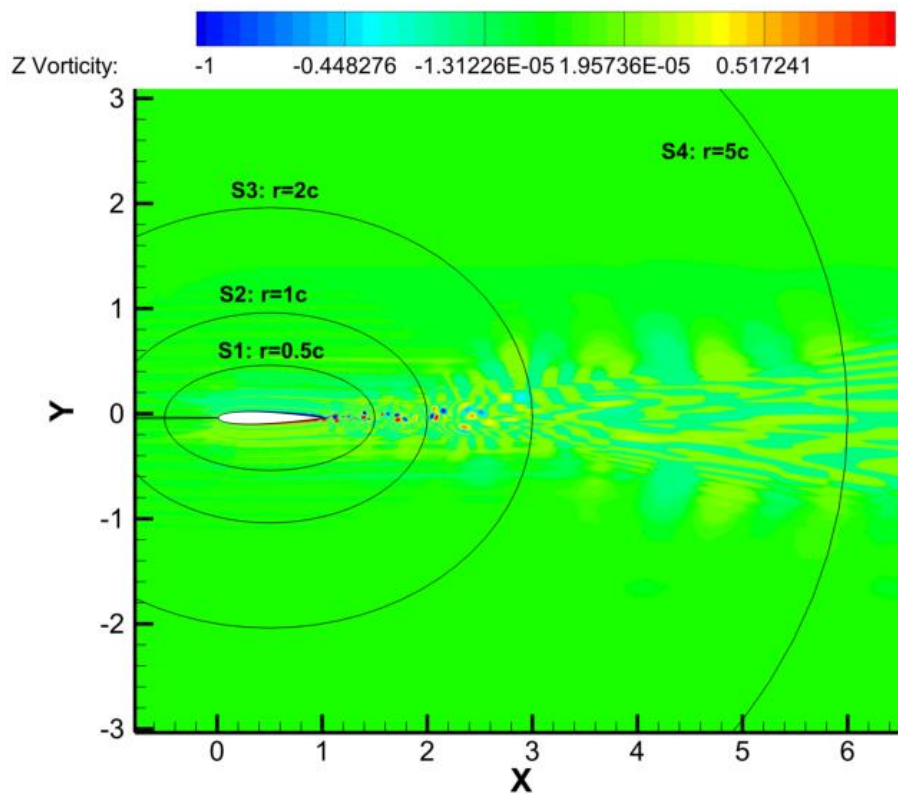


Figure 5.1 Velocity field obtained from CFD, superimposed with the control surfaces.

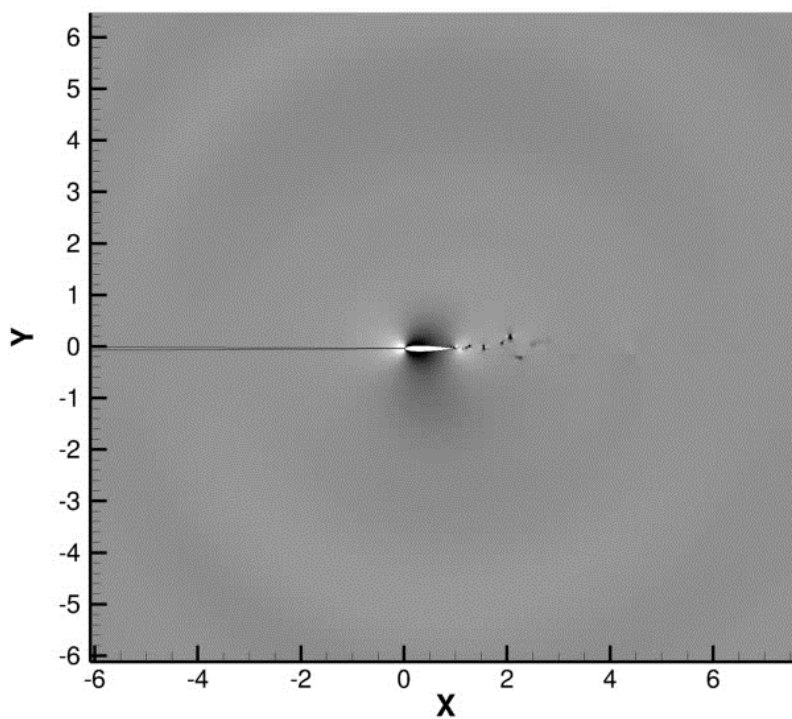


Figure 5.2 Pressure waves contour obtained from CFD

5.2. Acoustic predictions and comparisons with direct CFD results

In order to check the effect of using different control surfaces, the evaluated far-field results at 5 chord away from the airfoil surface are calculated and compared with the direct computations from CFD. The computational grid at dented surfaces S1 (0.5c), S2 (1c), S3 (2c) surfaces are fine enough so that the pressure wave signal can be resolved on these surfaces. The S3 surface has 8-10 points per wavelength corresponding to cut off frequency of 10,000 Hz which seems to have enough points to resolve the signal.

Figure 5.2 shows the predicted acoustic spectra using different surfaces both for PTM and FW-H approaches in logarithmic scale. The acoustic pressure has been calculated at an observer point probed at 5 chords length away from the airfoil surface and above mid-chord ($R = 5$, $\theta = 90^\circ$ in polar coordinates). It can be observed a sudden drop in the broadband noise pattern after a certain frequency. This is caused by the grid resolution required to resolve the higher frequencies. For example for surface there are 7 to 8 points per wave length to resolve up to the 10,000 Hz frequency and anything above that cannot be resolved. The cut-off frequency for different surfaces is near the specified black line on the logarithmic spectra plots.

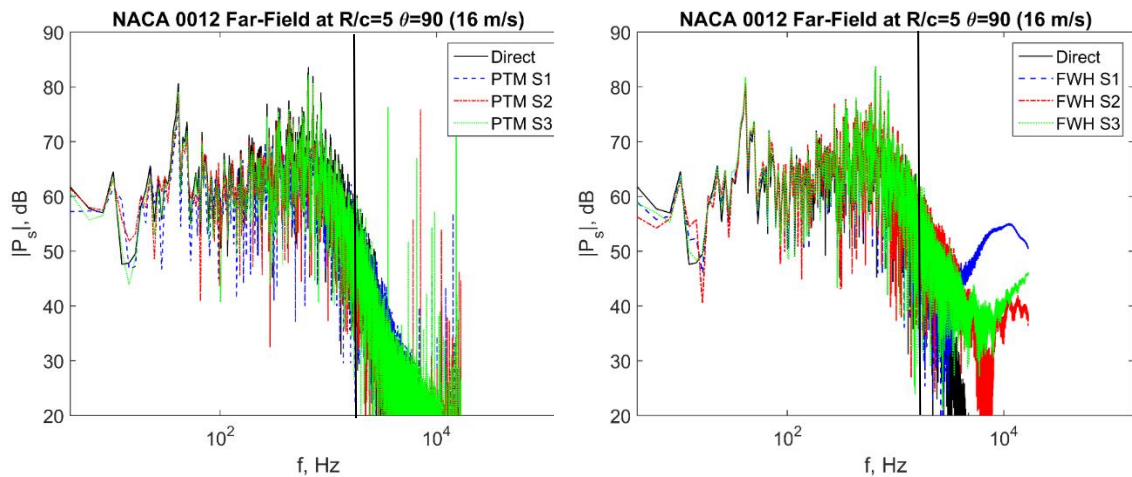


Figure 5.3 Logarithmic scale SPL spectra at $R/c = 5$ and $\theta = 90^\circ$ using S1, S2, and S3

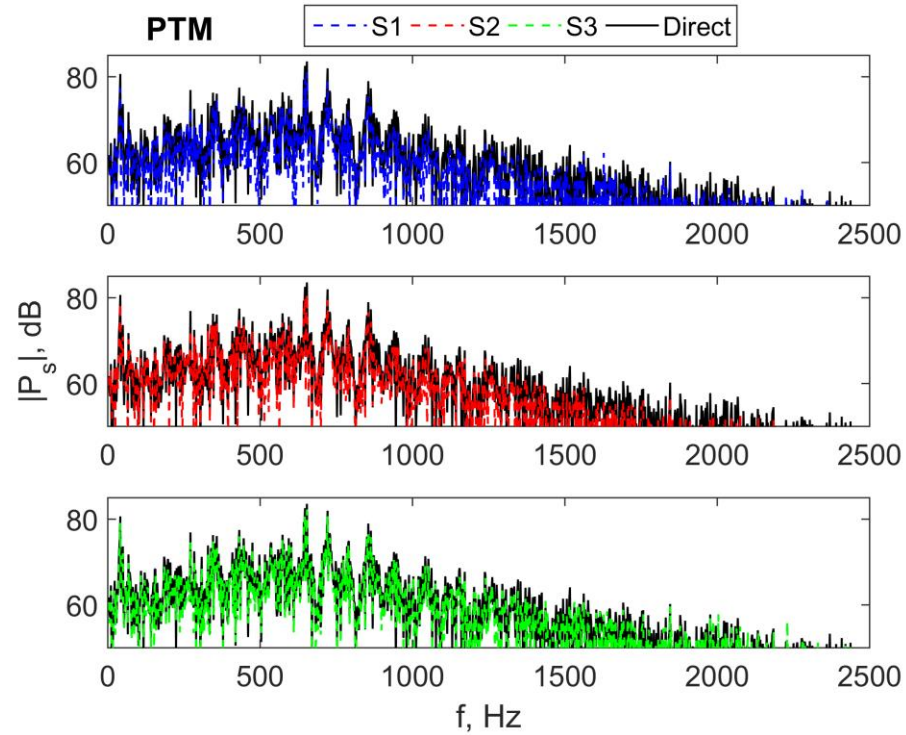


Figure 5.4 Acoustic spectra at $R/c = 5$ and $\theta = 90^\circ$ using S1, S2, and S3 surfaces obtained from PTM

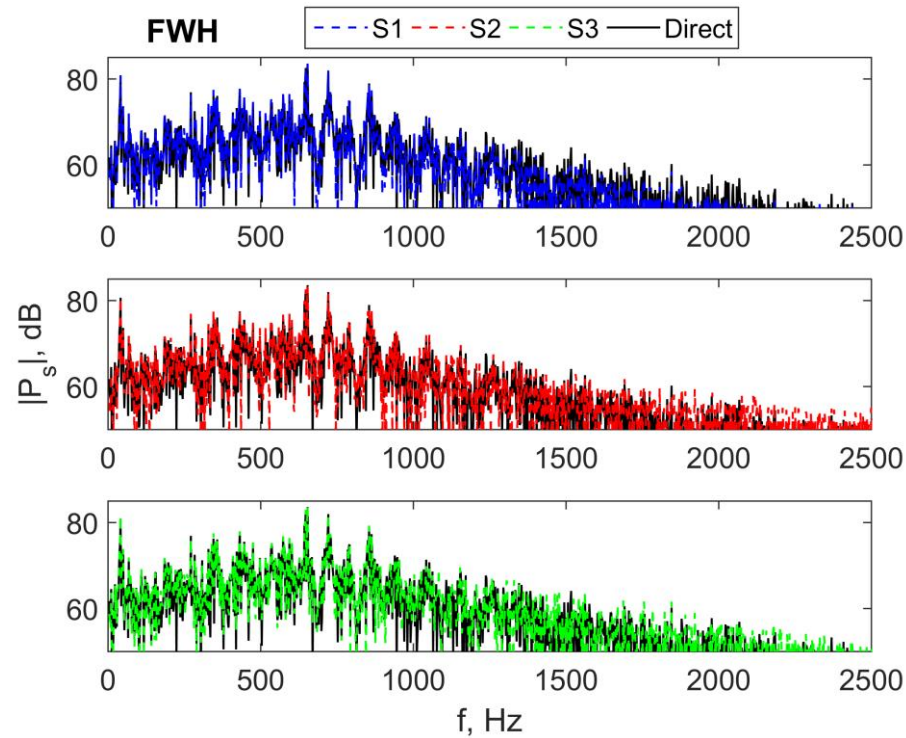


Figure 5.5 Acoustic spectra at $R/c = 5$ and $\theta = 90^\circ$ using S1, S2, and S3 surfaces obtained from FW-H

The acoustic spectra using different surfaces and their one by one comparison with the direct signal obtained from CFD is illustrated in Figure 5.4 and Figure 5.5 for PTM and FW-H approaches respectively. Both methods show good match with the direct signal. In the PTM method, the S3 surface shows a better match with the experiment compared to other surfaces. Since the acoustic spectra are scaled in the dB levels, the differences in acoustic pressure are difficult to observe. The acoustic pressure directivities are obtained to exhibit the behavior of acoustic pressure using different integration surfaces.

Figure 5.6 and Figure 5.7 show the peak tone directivities and the RMS acoustic pressure directivities.

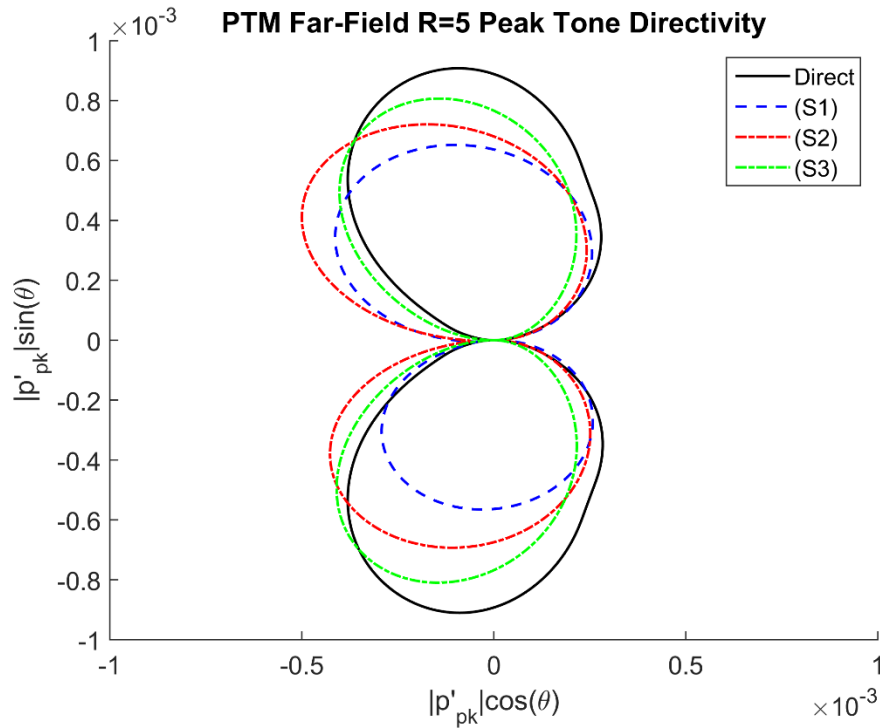


Figure 5.6 Peak tone directivity at $R/c = 5$ using S1, S2, and S3 surfaces obtained from PTM

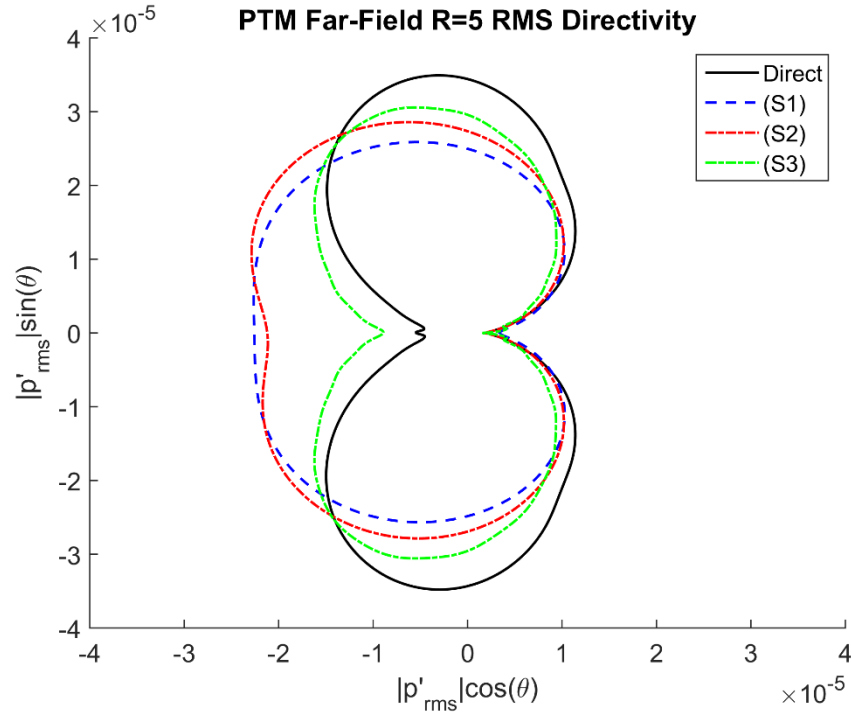


Figure 5.7 RMS directivity at $R/c = 5$ by S1, S2, and S3 surfaces obtained from FW-H

The peak tone and RMS pressure directivity results corresponding to the PTM confirms that the control surface should be far enough from the solid surface to include all the nonlinear effects and evaluate the propagated signal properly. This is because the PTM is a solution to the wave equation and following the Kirchhoff formulation, the Kirchhoff surface is assumed outside the nonlinear region. This can be illustrated by studying the pressure signals calculated directly from the CFD simulations.

Figure 5.8 shows the behavior of the RMS pressure directly calculated from the CFD simulations along the black straight line starting from the mid-chord on the surface up to 5 chords away. It can be observed that the RMS pressure disturbance variations after 3 chords away from the solid surface show a more linear pattern.

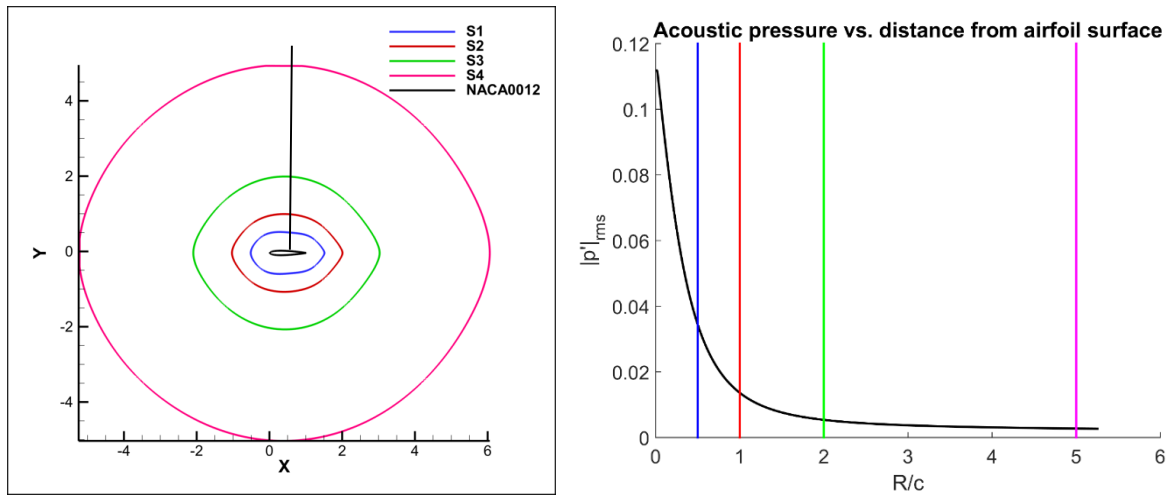


Figure 5.8 RMS pressure variations in radial direction computed from CFD simulations

The peak tone directivity and the RMS acoustic pressure directivities using surfaces S1, S2, and S3 are illustrated in Figures 5.9 and 5.10

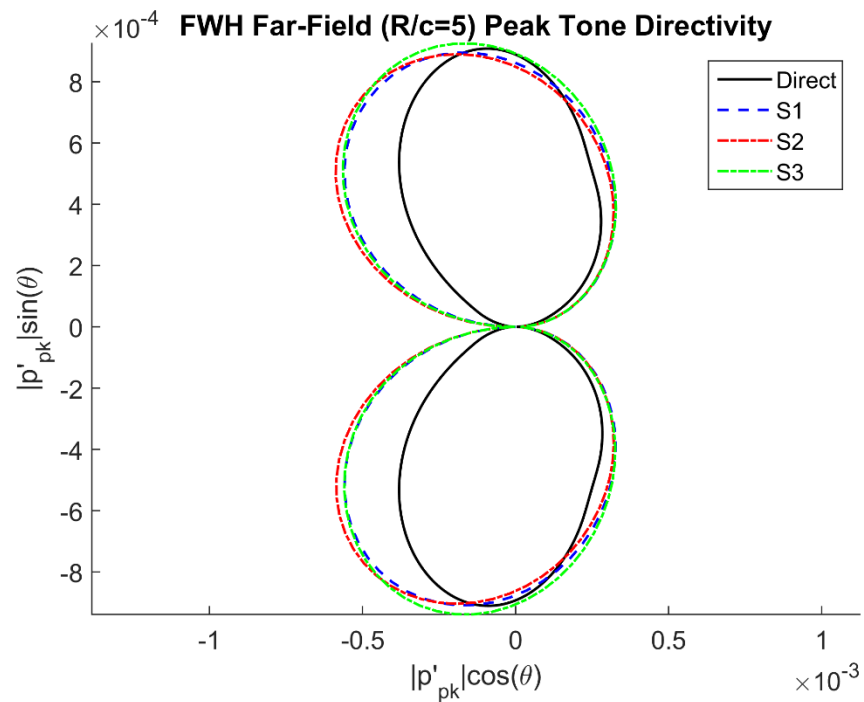


Figure 5.9 Peak tone directivity at $R/c = 5$ using S1, S2, and S3 surfaces obtained from FW-H

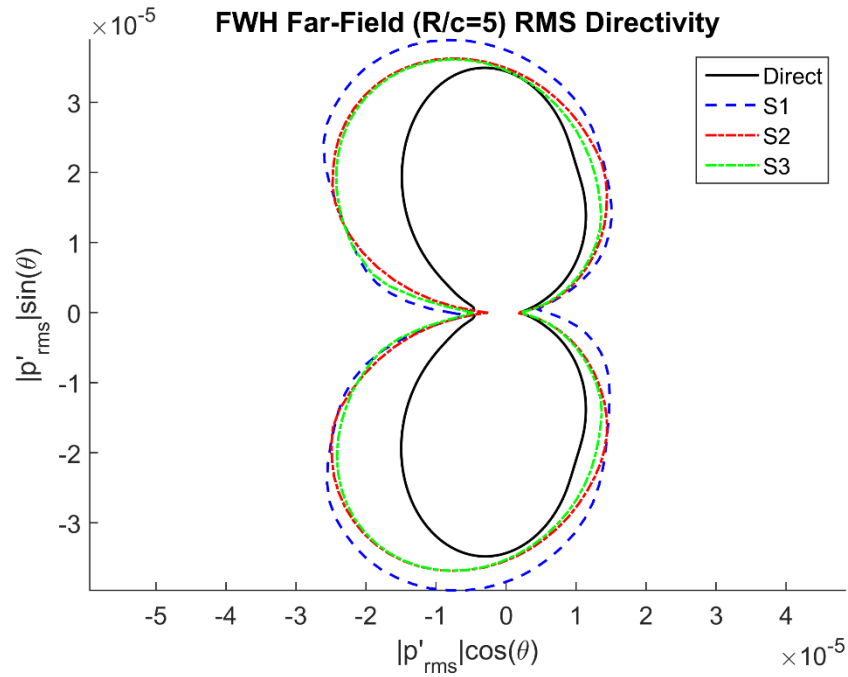


Figure 5.10 RMS directivity at $R/c = 5$ using S1, S2, and S3 surfaces obtained from FW-H

The peak tone directivities and RMS reassured directivities obtained from FW-H method exhibit relatively good agreement with the direct calculations. As expected, the FW-H method is less dependent on the placement of control surface and using the control surface in the nonlinear region does not propagate the nonlinear effects as acoustic sources. The robustness regarding the choice of control surface in FW-H methods has been addressed by earlier comparisons of FW-H and Kirchhoff method in several studies such as Lyrantzis (A. Lyrantzis 2003) and Brentner and Farassat (Kenneth S and Farassat 1997).

Comparing directivity results achieved by employing PTM and FW-H methods, it can be deduced that the PTM predicts the far-field acoustics properly only when the Kirchhoff surface is located outside the near-field region and encloses all the nonlinear effects. Figure 5.11 shows that both PTM and FW-H show a reasonable match with direct

calculations especially in predicting the tonal acoustics when the surface is outside the nonlinear region.

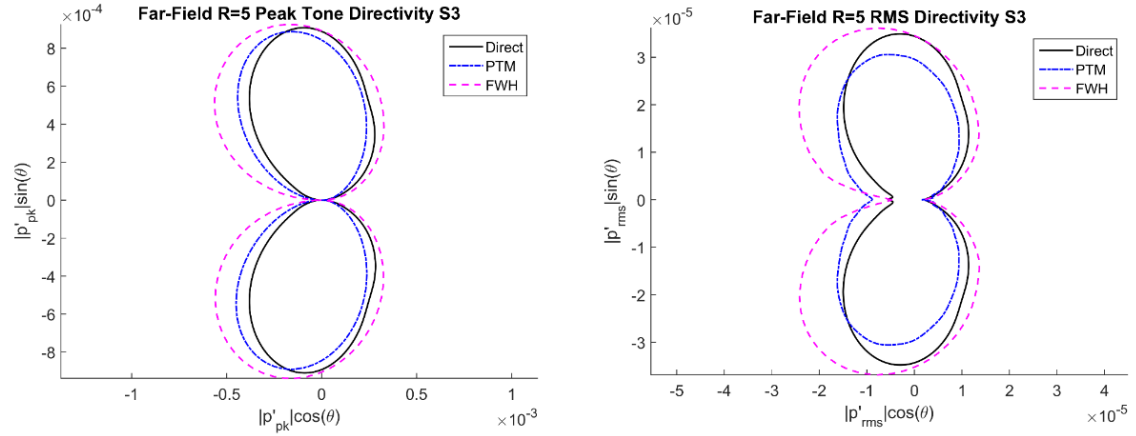


Figure 5.11 Peak and RMS directivity at $R/c = 5$ using S3 surface

As a general discussion about directivity of the noise from airfoil, the results show a dipole pattern that confirms the dipole nature of the problem and is caused by the varying force on the solid surface which is considered as the main noise source in dipole problems which has been mentioned in several references such as Lighthill (Michael James Lighthill 1954). Figure 5.12 illustrates the time history and the FFT of lift and drag coefficients. It can be comprehended that the variation of force acting on airfoil gives rise to dipole acoustic signature. Comparing the amplitudes of the peak harmonics of lift and drag coefficients in Figure 5.12, it can be observed that for a symmetric airfoil, contribution of lift is higher than the contribution of drag as an indication of cause of dipolar acoustic structure.

Some of the differences especially in the FW-H directivities are probably due to the passage of the strong vertical structure through the integration surfaces that is also contributing to the noise. The apparent noise is caused by a time varying force that passes

the integration surface the vortex structure. This noise would be cancelled out if the quadrupole terms were included. Although the noise generated by the lift variation on the airfoil dominates the contribution of this problem, but care must be taken to make sure that the fake sources in the wake do not contaminate the results which is also mentioned by Lockard (Lockard 2000) for the application of FW-H to cylinder shedding noise.

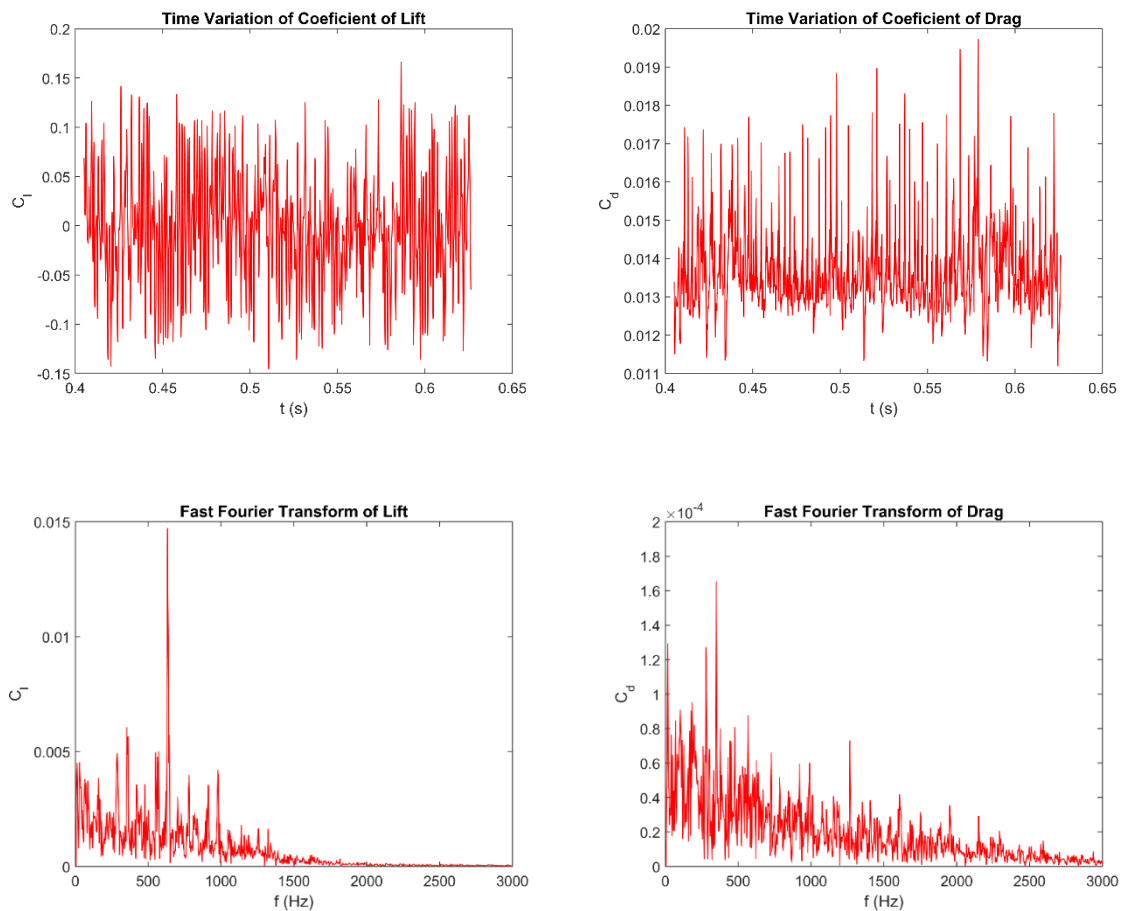


Figure 5.12 Time history and Fast Fourier transform of lift and drag coefficients

Another approach in investigating the directivity results, is to plot the RMS pressure in terms of dB level scale. The acoustic sound pressure level in dB level scale is shown in terms of polar angle in the directivity plane in Figure 5.13. It can be observed

that both PTM and FW-H show a reasonable match in terms of Sound Pressure Level (dB scale). For PTM, using the S3 surface shows a better match with direct results while the FW-H is less sensitive to choice of control surface, which is what was inferred from directivity results previously.

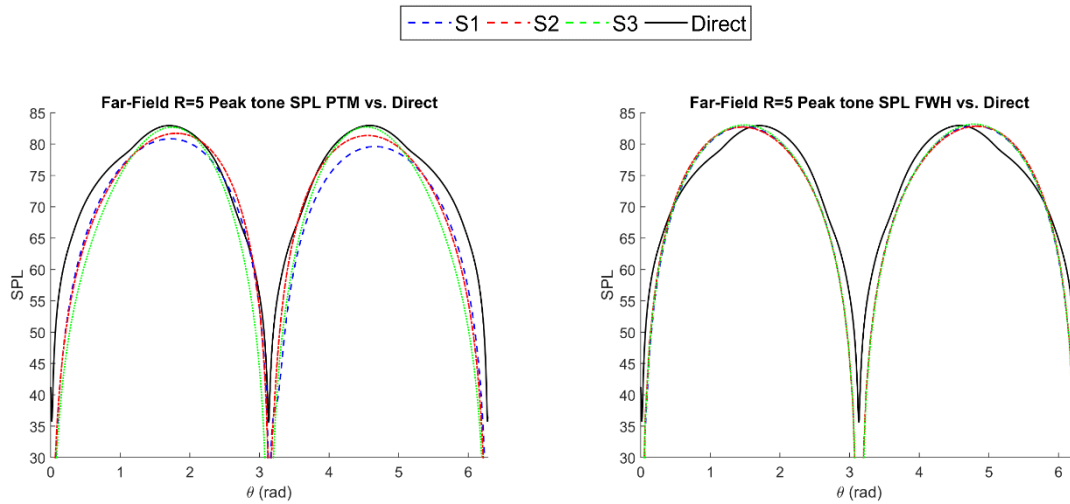


Figure 5.13 Peak tone sound pressure level in terms of directivity angle.

5.3. Acoustic predictions and comparisons with experiment

In order to compare the far-field acoustic spectra with the experimental results, the acoustic predictions using the FW-H and PTM are evaluated at probe point at 12.5 chords away from the airfoil surface and above mid-chord ($R = 12.5$, $\theta = 90^\circ$ in polar coordinates). It has been demonstrated that for the PTM the Kirchhoff surface should be located outside the near-field region and encloses all the nonlinear effects. Also for FW-H methods S3 surface shows slightly better results especially for the RMS directivities. The surface S3 has been used for predictions at 12.5c and comparisons with experiment.

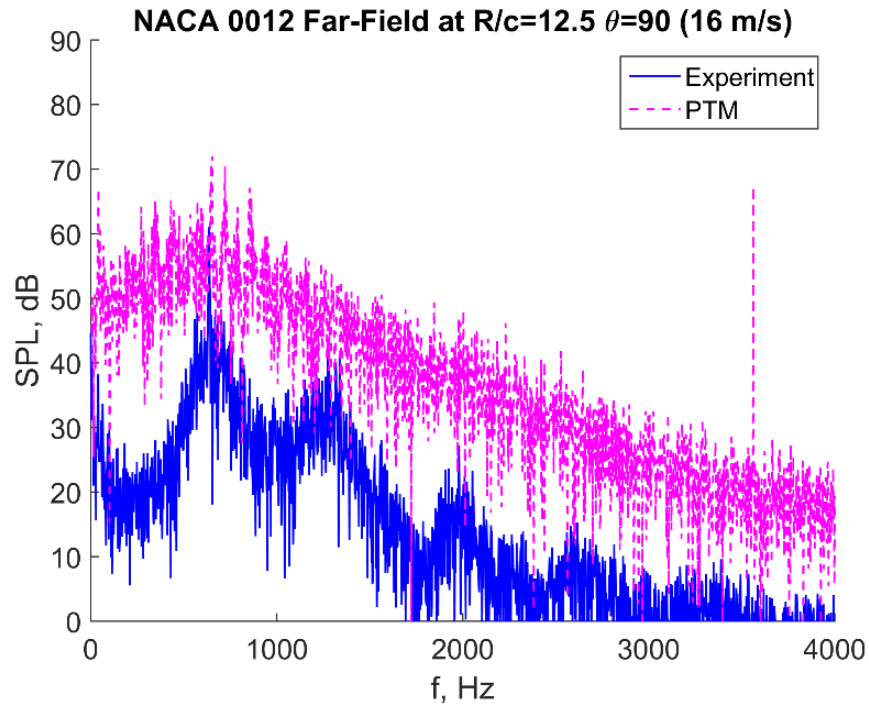


Figure 5.14 Acoustic Spectrum at $R/c = 12.5$ (PTM) without Correction

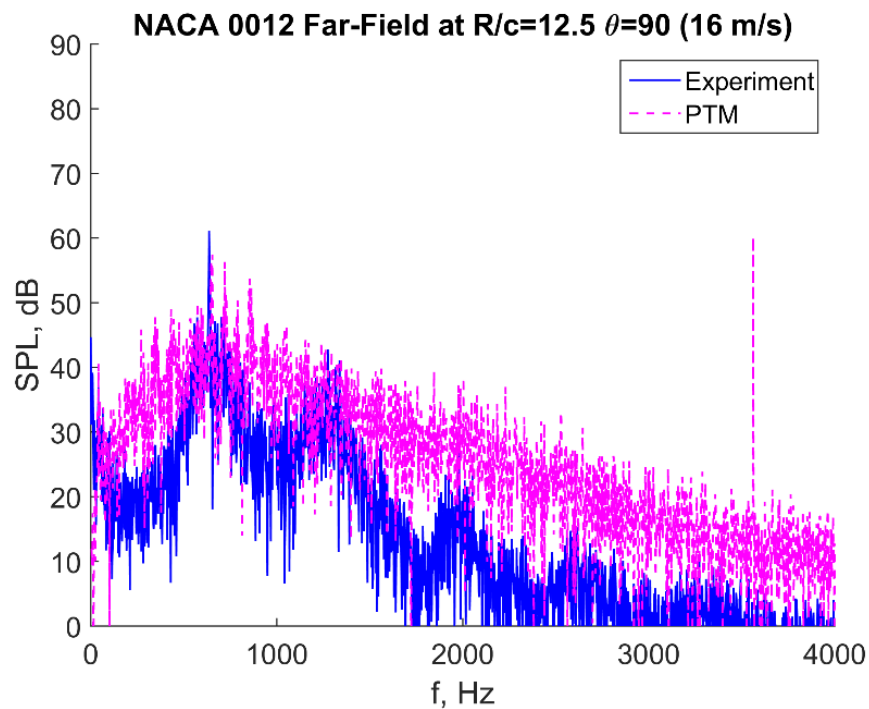


Figure 5.15 Acoustic Spectrum at $R/c = 12.5$ (PTM) with Correction

Figure 5.14 shows the comparison of the evaluated noise signal using PTM and experiment. It can be observed the pattern of the spectrum is very close to the

experiment, but the levels are higher. This is caused because sound pressure level measured directly in the simulation contains contributions from mirrored coherent image sources of the airfoil arriving through the cyclic domain boundaries to the microphone location, also mentioned by Valden et al (van der Velden et al. 2015). To correct this Oberai's correction has been used. This correction factor is a frequency dependent factor to normalize the acoustic spectrum shift caused by periodic boundary condition in numerical methods.

For this study, the three dimensional numerical data is computed numerically and averaged throughout the entire span. The resulting pseudo-two dimensional results have been evaluated by FW-H and PTM methods. Figure 5.16 and Figure 5.17 show the two dimensional and span averaged three dimensional results for PTM and FW-H methods. The three dimensional CFD results are averaged along the span such that as the result, a plane two dimensional input can be used in the two dimensional integral methods. Comparing two dimensional data and the three dimensional span averaged data with experiment, the three dimensional results better represents the broad noise pattern.

The numerical results compare well with experiments as peak frequencies are accurately captured and broadband levels are of the same amplitudes at frequencies adjacent to the main tone. As expected, 3D ILES exhibit a near perfect match to experiment between 500-1500Hz whereas 2D results slightly over-predicts the broadband at lower frequencies. Results PTM compares slightly better with experiment in predicting the broadband noise pattern, whereas the FW-H method captures the peak tone frequency and amplitude better than PTM.

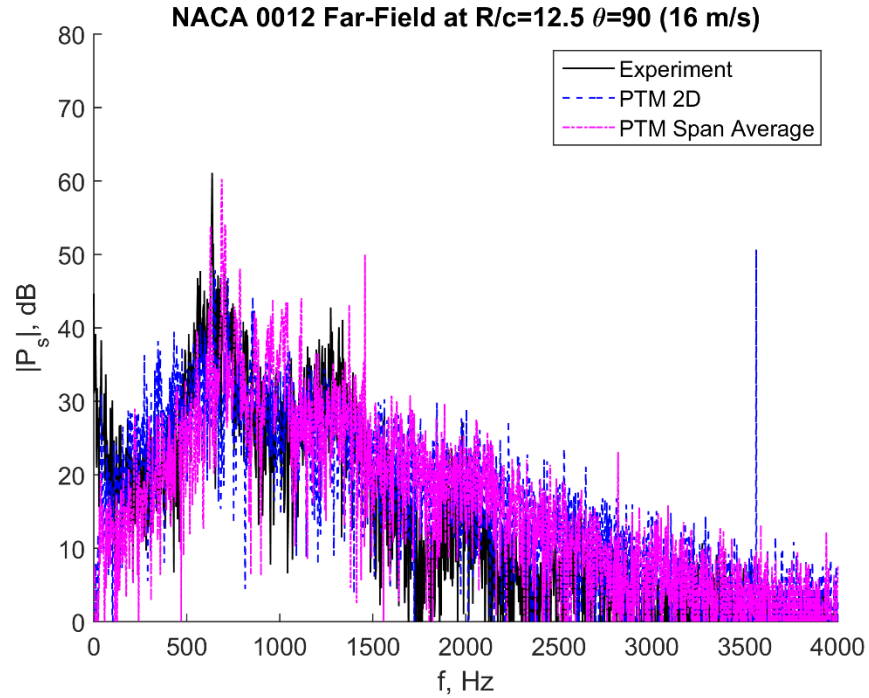


Figure 5.16 Acoustic Spectrum at $R/c = 12.5$ two dimensional and span averaged three dimensional data employed for PTM method and comparison with Experiment

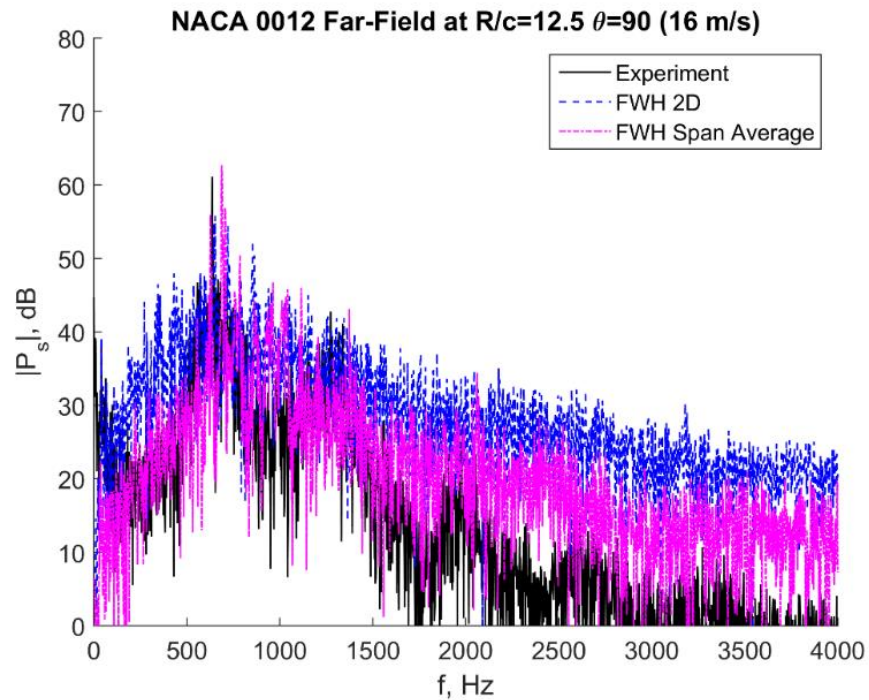


Figure 5.17 Acoustic Spectrum at $R/c = 12.5$ two dimensional and span averaged three dimensional data employed for FW-H method and comparison with Experiment

Studying the spectrum graphs, reveals the need to reduce the fluctuation noise caused by insufficient data samples for the FFT process. Useful signal processing technique of sample averaging is enhanced in the developed codes to reduce the numerical noise caused by FFT process. In order to apply sample averaging, two times longer time history of the flow variables are collected. For the PTM approach the pressure signal is divided into 4 segments and FFT is applied on each segment. Then the frequency domain data from each segment are summed together and averaged and used as input for far-field prediction. The same approach is applicable for the FW-H method as well. It is very important to note that the FW-H formulation is linear in terms of the F_i and Q , so the FFT and averaging technique should be applied to these terms after they are calculated from flow variables. As it is illustrated in Figure 5.18, the evaluated signal using the traditional way is very noisy and causes some difficulty to investigate the patterns of the acoustic spectra. The averaging technique increases the resolvable frequency for the FFT procedure by dividing the time data in 4 and reduces the computational noise. The acoustic predictions from both method using the averaged data clearly shows consistent pattern for the broadband as well as peak tone compared with experiment.

Figure 5.19 shows the calculated RMS acoustic pressure and peak tone directivities obtained from PTM and FW-H formulations. The directivity plots show that with the correct choice of control surface and appropriate signal processing tools, both methods provide very similar predictions of the far-field acoustics.

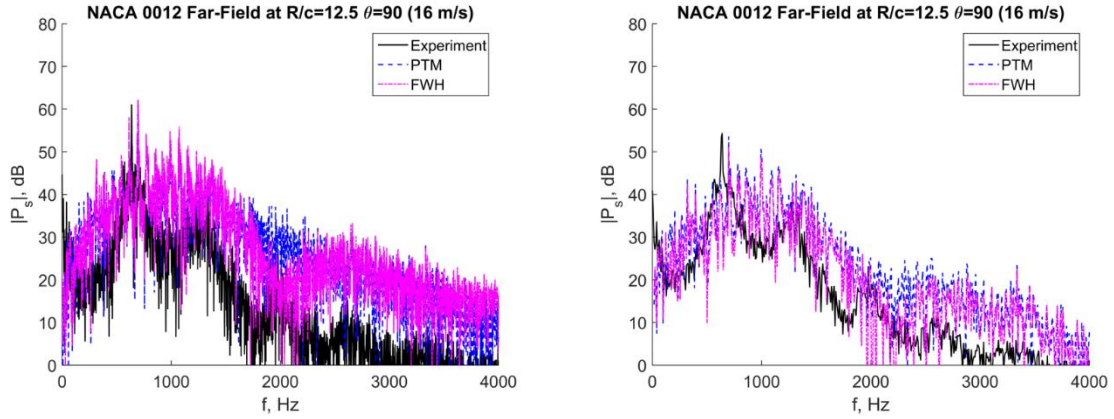


Figure 5.18 Acoustic Spectrum at $R/c = 12.5$ of the long time signal, without averaging (Left) and with averaging (Right)

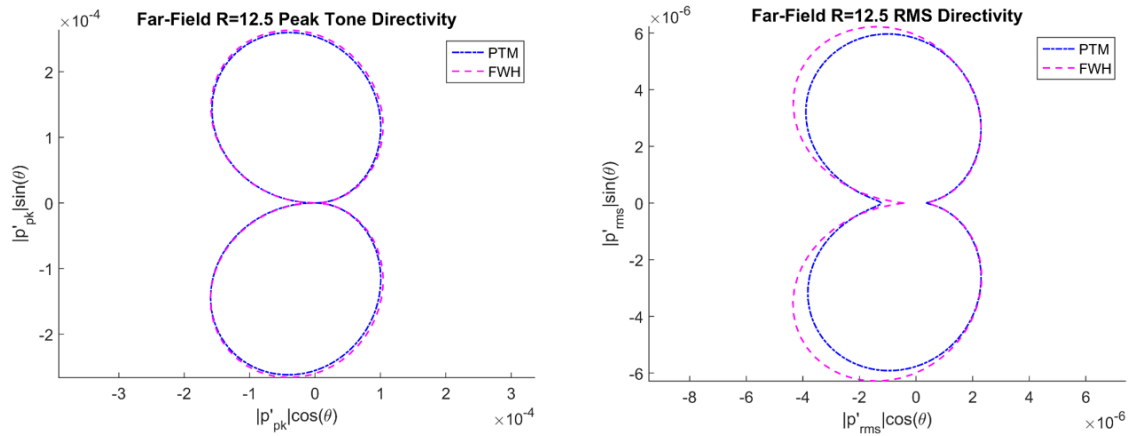


Figure 5.19 Peak tone directivities (Left) and RMS acoustic pressure directivities (Right) from PTM and FW-H methods at the observer radius of $R/c = 12.5$

In Figure 5. 20, the acoustic intensities are calculated along the 90 degree line on top of the airfoil at different control surfaces S1, S2, S3, S4 and the observer radius at 12.5 chords away. The calculated intensities at 4 surface from CFD calculations as well as the evaluated acoustic intensity at the far-field radius from both methods, exactly follow the inverse square law relation with the distance from the airfoil. It is clear that the air foil in the two-dimensional domain behaves as an acoustic source, and both PTM and FW-H methods provide the acoustic pressure solution for the linear propagation of pressure governed by the wave equation.

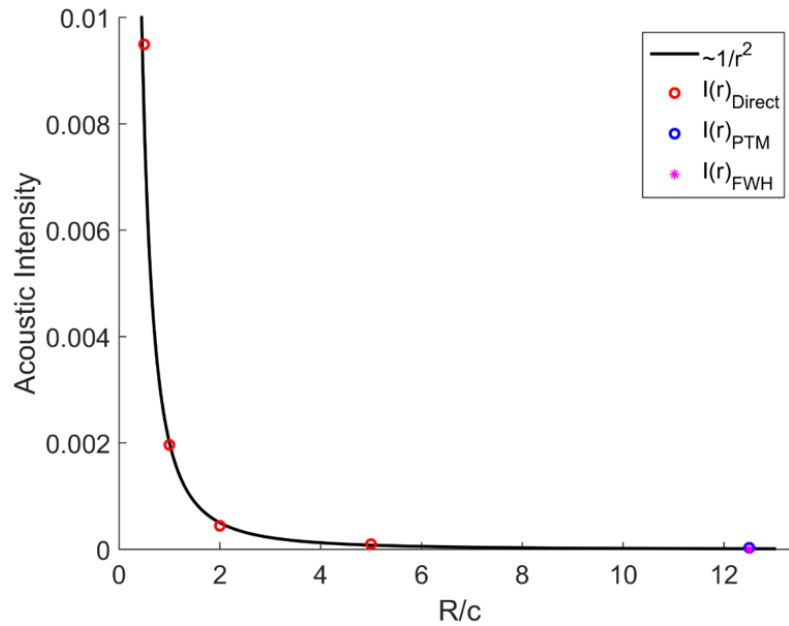


Figure 5.20 Acoustic intensity calculate at S1, S2, S3, S4, and observer circle at 12.5c

5.4. Tonal acoustic studies of variation of angle of attack

The developed methods to predict the far-field acoustics along with the high accuracy results show good results in prediction of tonal noise and the corresponding frequency. Presented here is the case of Re of 180,000, but at varied incidence angles. The range of angle of incident can be split into two distinct regions of tone generating and no-tone generating regimes. This range is indicated by the red line on figure 5.12. The objective is to provide spectrum of far-field noise along with linear stability studies(Golubev et al. 2013) to confirm the tone generating regime for variation of angle of attack

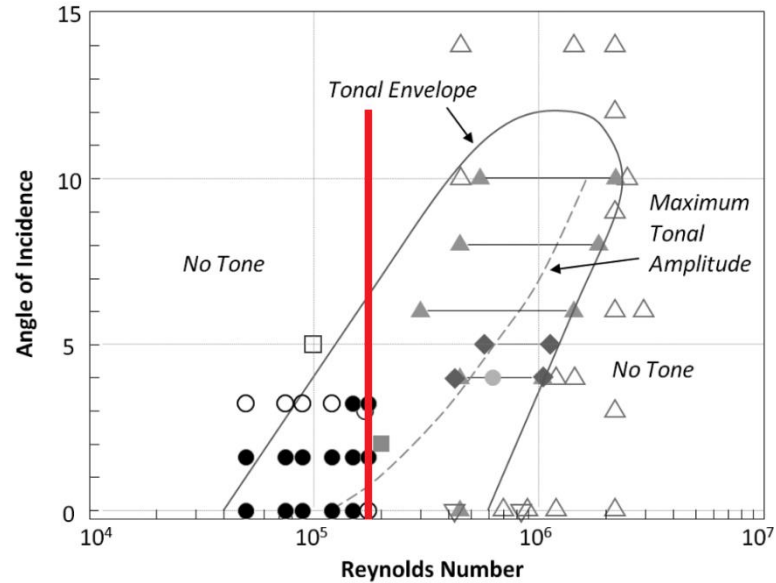


Figure 5.21 Varying angle of attack for fixed $Re = 180,000$ (Arcondoulis et al. (Arcondoulis et al. 2013))

Based on the presented tonal envelope in Figure 5.21, it is expected that tonal noise can be observed starting at 0° and continuing as high as 6° . Filled markers represent that a tone was present, while unfilled markers represent that a tone was not present. Data sources: circles (Arcondoulis et al. (Arcondoulis et al. 2013)), triangles (Paterson et al. (Paterson et al. 1973)), inverted triangles (Arbey and Bataille (Arbey and Bataille 1983)), squares, (Desquesnes et al. (Desquesnes, Terracol, and Sagaut 2007)), diamonds (Lowson et al. (Lowson, Fiddes, and Nash 1994)), Tonal envelope and maximum amplitude line (Lowson et al. (Lowson, Fiddes, and Nash 1994)).

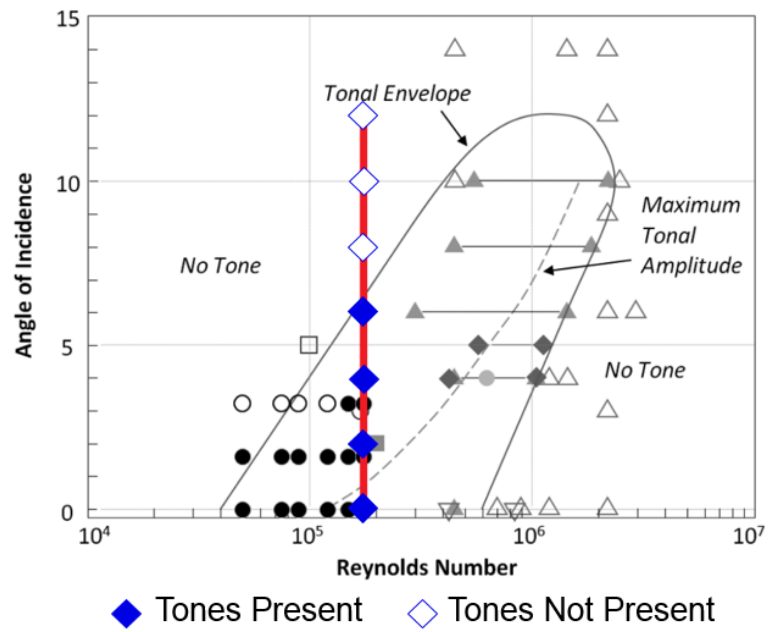


Figure 5.22 Presence of tones for varied angle of attack

Angle	Frequency (Hz)	Sound Pressure Level (dB)
0	1550	95.7
2	2323, 1156	85.1, 79.4
4	1247	85.0
6	1209	90.5

Table 5.1 Far-field peak tonal frequencies by case

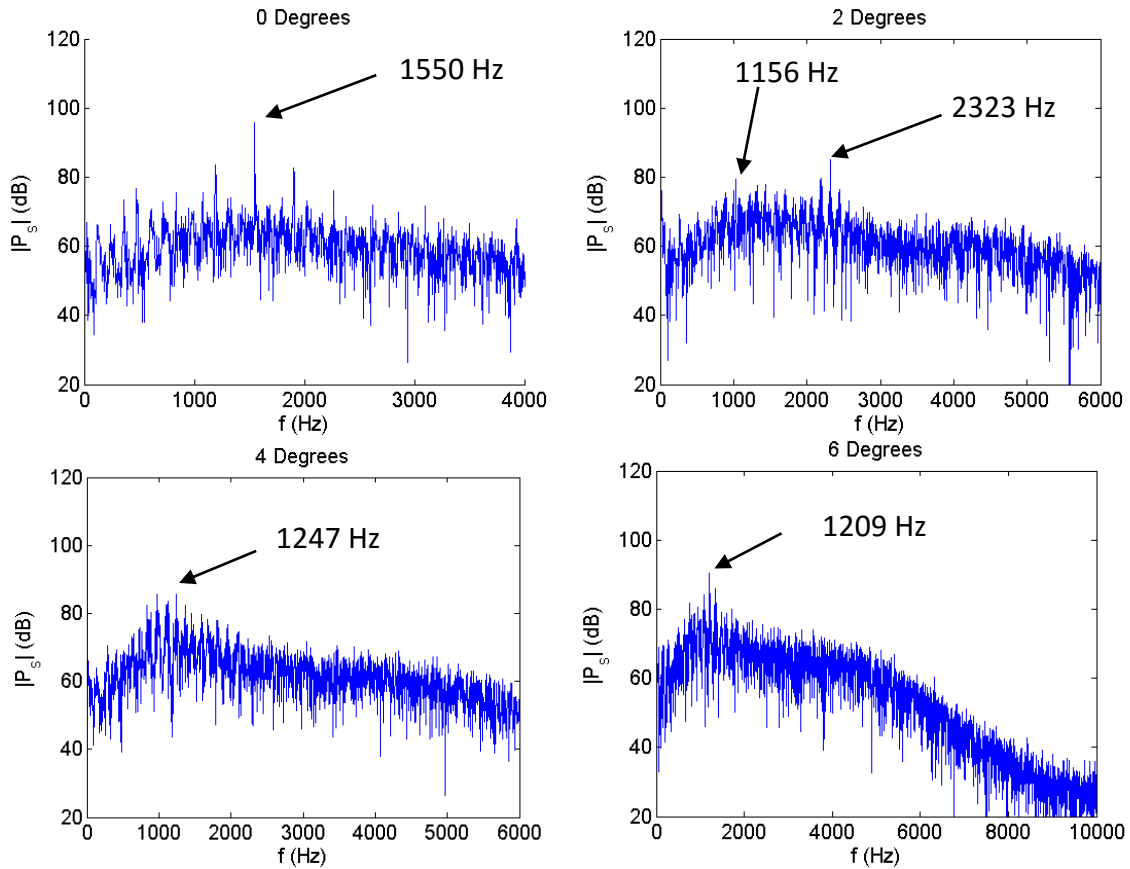


Figure 5.23 Far-field acoustic spectra for cases with tonal peaks at 0°, 2°, 4°, 6°.

The far-field acoustic spectrum for each incidence angle is given in Figure 5.21. These far-field spectra were generated for an observer at 12.5 chords above the trailing edge by the FW-H method using a control surface at 2 chord away from the airfoil surface using flow variables fluctuation data from the ILES code results. At 0°, 2°, and 6°, and slightly clear at 4°, clear tonal peaks can be observed in the far-field. The exact frequencies and intensities of these peaks are listed in Table 2.1.

As expected, no tonal peaks are observed at 8°, 10°, or 12°, whose spectra are given in Figure 5.15. Only broadband trends are observed at these angles.

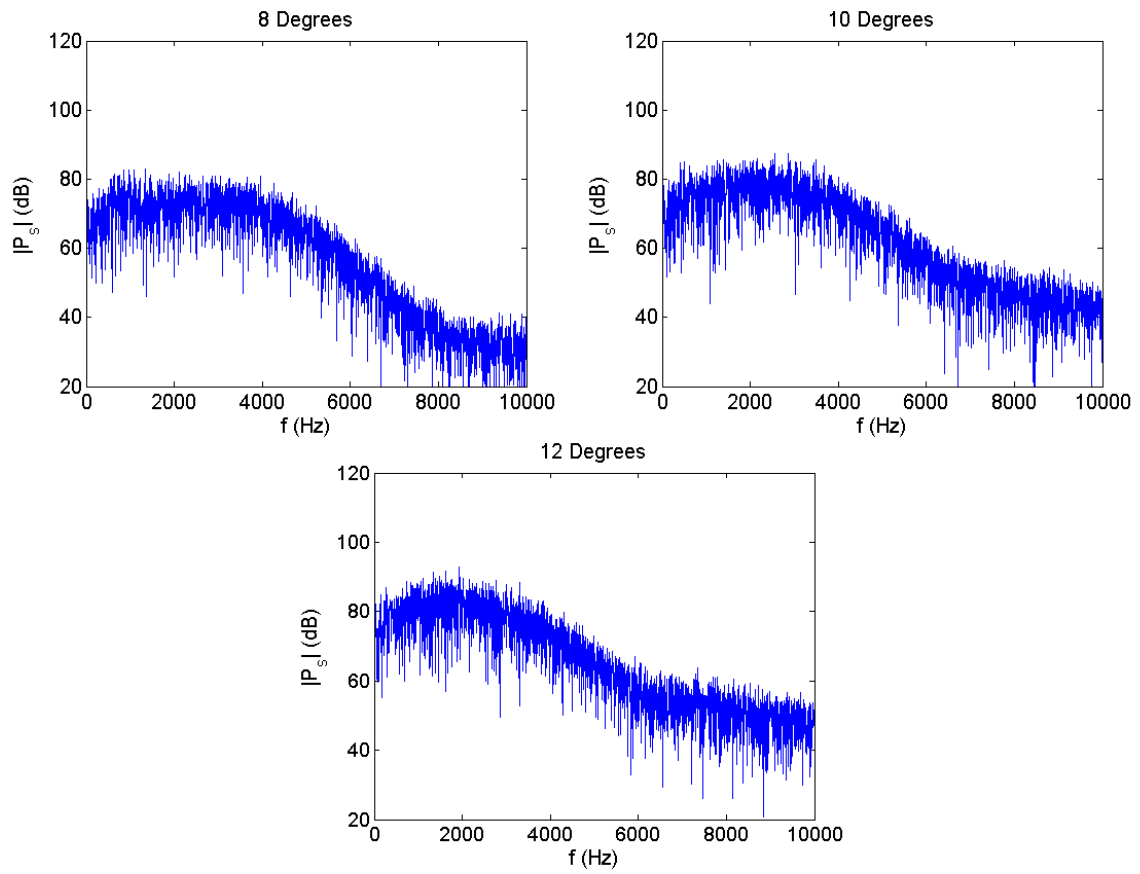


Figure 5.24 Far-field acoustic spectra for cases without tonal peaks

6. Conclusions and Recommendations

High-accuracy 2D and 3D (ILES) numerical experiments were conducted to investigate the phenomenon of flow-acoustic resonant interactions at moderate Reynolds number characteristic of a transitional airfoil. A high-fidelity viscous solver along with surface integral codes were employed to predict and conduct comparison study between two dimensional FW-H formulation and PTM framework.

Comparing the formulations and numerical implementation process, it has been concluded that PTM's simplified equations are easy to implement. However, the effort to transition from 2D to 3D formulation while eliminating the normal derivatives is relatively difficult. On the other hand, although the FW-H formulation requires more effort to implement in normal vectors of the source terms and the derivative of the Green's function, but the formulation is more compatible with three dimensional problems and there has been successful implementations for three dimensional problems by many researchers.

PTM requires pressure time data on the Kirchhoff surface, whereas the FW-H requires all the flow variable time data to calculate the source term groupings, hence requires more memory size for numerical computations. Working with high fidelity CFD results, usually introduces difficulties in the post-processing the near-field data using FW-H method. Because the extensive amount of data requires more computing time for read/write process of data as well as storing the input and output of the solution. Hence FW-H requires more memory. On the other hand, in the numerical implementation of PTM a matrix of the size

of number of points on the surface needs to be evaluated in order to solve the aforementioned system of equations. For higher number of points on the matrix evaluation requires higher amount of CPU time, which make this method less efficient compared to the FW-H method.

Conducting monopole source validation confirms the capability of both methods to predict the acoustic pressure for a simple model problem. Also the accuracy of both developed numerical code have been tested by the model problem.

Throughout the numerical experiment and comparisons with the direct results at $5c$ away from airfoil surface (where CFD results are still reliable), it has been demonstrated that PTM predicts the acoustic pressure only when the Kirchhoff surface is not in the nonlinear region. This caused by the initial assumption made in the original governing equation for PTM and Kirchhoff methods in general. In the PTM approach the linear Wave/ Helmholtz equation is solved in a linear region while the main assumption is that the surface places in the linear region and encloses all nonlinear effects. On the contrary the FW-H has been proven and demonstrated in this study, correctly filters out the most of the nonlinearities especially where the quadrupole terms are not significant.

Studying the spectrum graphs, demonstrated the need to reduce the fluctuation noise caused by insufficient data samples for the FFT process. With the use of proper signal processing techniques the numerical noise in the spectra results can be reduced which not only helps to observe the peak frequency, but also makes the investigation of the broad band pattern more understandable. In the

case of comparison with experiment, using the averaging method applied to the input signal for both PTM and FW-H methods, caused better match between far-field noise and the experimental data.

The pseudo-two dimensional numerical experiments confirm that the 2D acoustic propagation formulations can be useful as preliminary studies of the acoustic problems and can augment full three dimensional whenever higher accuracy is required for the predictions.

REFERENCES

- Arbey, H, and J Bataille. 1983. "Noise Generated by Airfoil Profiles Placed in a Uniform Laminar Flow." *Journal of Fluid Mechanics* 134. Cambridge Univ Press: 33–47.
- Arcondoulis, E, C Doolan, A Zander, and L Brooks. 2013. "An Experimental Investigation of Airfoil Tonal Noise Caused by an Acoustic Feedback Loop." In *Proceedings of Acoustics*.
- Atassi, H M, M Dusey, and C M Davis. 1993. "Acoustic Radiation from a Thin Airfoil in Nonuniform Subsonic Flows." *AIAA Journal* 31 (1): 12–19.
- Atassi, Hafiz M, Shankar Subramaniam, and James R Scott. 1990. "Acoustic Radiation from Lifting Airfoils in Compressible Subsonic Flow." In *AIAA, Space Programs and Technologies Conference*. Vol. 1.
- Crighton, D G, Ann P Dowling, J E Ffowcs Williams, M A Heckl, and F A Leppington. 2012. *Modern Methods in Analytical Acoustics: Lecture Notes*. Springer Science & Business Media.
- Desquesnes, G, M Terracol, and P Sagaut. 2007. "Numerical Investigation of the Tone Noise Mechanism over Laminar Airfoils." *Journal of Fluid Mechanics* 591. Cambridge Univ Press: 155–82.
- Di Francescantonio, P. 1997. "A New Boundary Integral Formulation for the Prediction of Sound Radiation." *Journal of Sound and Vibration* 202 (4). Elsevier: 491–509.
- Du, Yongle, and Philip J Morris. 2014. "Accurate and Efficient Jet Flow and Noise Simulations Using the CDE (Compact Disturbance Equations)." *AIAA Paper* 2602: 2014.
- Farassat, F. 2001. "Acoustic Radiation from Rotating Blades—the Kirchhoff Method in Aeroacoustics." *Journal of Sound and Vibration* 239 (4). Elsevier: 785–800.
- Farassat, F, and M K Myers. 1988. "Extension of Kirchhoff's Formula to Radiation from Moving Surfaces." *Journal of Sound and Vibration* 123 (3). Elsevier: 451–60.
- Farassat, Feri. 1981. "Linear Acoustic Formulas for Calculation of Rotating Blade Noise." *AIAA Journal* 19 (9): 1122–30.
- George, A R, and A S Lyrantzis. 1986. "Mid-Field and Far-Field Calculations of Blade-Vortex Interactions." In *Thermophysical Aspects of Re-Entry Flows*. Vol. 1.
- Golubev, Vladimir V, Lap Nguyen, R R Mankbadi, M Roger, C Pasiliao, and M R Visbal. 2014. "Effect of Upstream Turbulence on Flow-Acoustic Resonant Interactions in Transitional Airfoils." *AIAA Paper* 3303.

- Golubev, Vladimir V, Lap Nguyen, Reda R Mankbadi, Michel Roger, and Miguel R Visbal. 2013. "Acoustic Feedback-Loop Interactions in Transitional Airfoils." *AIAA Paper* 2111.
- Golubev, Vladimir, Lap Nguyen, Warren Hiner, Marco Sansone, Saman Salehian, Reda Mankbadi, Gyuzel Yakhina, and Michel Roger. n.d. "Parametric Investigations of Tonal Trailing-Edge Noise Generation by Moderate Reynolds Number Airfoils Part II—Numerical Studies."
- Hariharan, S I, and R C MacCamy. 1986. "Low Frequency Acoustic and Electromagnetic Scattering." *Applied Numerical Mathematics* 2 (1). Elsevier: 29–35.
- Hariharan, S I, J R Scott, and K L Kreider. 2000. "A Potential-Theoretic Method for Far-Field Sound Radiation Calculations." *Journal of Computational Physics* 164 (1). Elsevier: 143–64.
- Hawkings, D L. 1979. "Noise Generation by Transonic Open Rotors." In *Mechanics of Sound Generation in Flows*, 1:294–300.
- Hsiao, George, and R C MacCamy. 1973. "Solution of Boundary Value Problems by Integral Equations of the First Kind." *SIAM Review* 15 (4). SIAM: 687–705.
- Kenneth S, Brentner, and F Farassat. 1997. "An Analytical Comparison of the Acoustic Analogy and Kirchhoff Formulation for Moving Surfaces." NASA Langley Technical Report Server.
- Lele, Sanjiva K. 1992. "Compact Finite Difference Schemes with Spectral-like Resolution." *Journal of Computational Physics* 103 (1). Elsevier: 16–42.
- Lighthill, Michael J. 1952. "On Sound Generated Aerodynamically. I. General Theory." In *Proceedings of the Royal Society of London A: Mathematical, Physical and Engineering Sciences*, 211:564–87. The Royal Society.
- Lighthill, Michael James. 1954. "On Sound Generated Aerodynamically. II. Turbulence as a Source of Sound." In *Proceedings of the Royal Society of London A: Mathematical, Physical and Engineering Sciences*, 222:1–32. The Royal Society.
- Lilley, G M. 1974. "On the Noise from Jets." *Agard Cp-131* 13: 12.
- Lockard, David P. 2000. "An Efficient, Two-Dimensional Implementation of the Ffowcs Williams and Hawkings Equation." *Journal of Sound and Vibration* 229 (4). Elsevier: 897–911.
- "A Comparison of Ffowcs Williams-Hawkings Solvers for Airframe Noise Applications." *AIAA Paper* 2580 (8).2002

- Lowson, M V, S P Fiddes, and E C Nash. 1994. "Laminar Boundary Layer Aeroacoustic Instabilities. AIAA Paper 94-0358." In *32nd Aerospace Sciences Meeting and Exhibition, Reno*.
- Lyrintzis, A S, and R Mankbadi. 1996. "Prediction of the Far-Field Jet Noise Using Kirchhoff's Formulation." *AIAA Journal* 34 (2): 413–16.
- Lyrintzis, A S, and A Uzun. 2001. "Integral Techniques for Jet Aeroacoustics Calculations." *AIAA Paper* 2253.
- Lyrintzis, Anastasios. 2003. "Surface Integral Methods in Computational aeroacoustics—From the (CFD) near-Field to the (Acoustic) Far-Field." *International Journal of Aeroacoustics* 2 (2). Multi Science Publishing: 95–128.
- Lyrintzis, Anastasios S. 1994. "Review: The Use of Kirchhoff's Method in Computational Aeroacoustics." *Journal of Fluids Engineering* 116 (4). American Society of Mechanical Engineers: 665–76.
- Mankbadi, R R, S H Shih, R Hixon, J T Stuart, and L A Povinelli. 1996. "Extension of Near Field to Far Field Noise Prediction." *AIAA Paper*, 96–2651.
- Mankbadi, Reda R, M Ehtesham Hayder, and Louis A Povinelli. 1994. "Structure of Supersonic Jet Flow and Its Radiated Sound." *AIAA Journal* 32 (5): 897–906.
- Mankbadi, Reda R, R Hixon, S H Shih, and L A Povinelli. 1995. *On the Use of Linearized Euler Equations in the Prediction of Jet Noise*. Vol. 106929. Lewis Research Center.
- Myers, M K, and J S Hausmann. 1990. "On the Application of the Kirchhoff Formula for Moving Surfaces." *Journal of Sound and Vibration* 139 (1). Academic Press: 174–78.
- Paterson, Robert W, Paul G Vogt, Martin R Fink, and C Lee Munch. 1973. "Vortex Noise of Isolated Airfoils." *Journal of Aircraft* 10 (5): 296–302.
- Pilon, Anthony Richard, and A Lyrintzis. 1997. "Development of Improved Surface Integral Methods for Jet Aeroacoustic Predictions." *NASA Technical Report No. NASA/CR-97-207181*, NASA, Washington, DC.
- Pletcher, Richard H, John C Tannehill, and Dale Anderson. 2012. *Computational Fluid Mechanics and Heat Transfer*. CRC Press.
- Salomons, Erik M. 2012. *Computational Atmospheric Acoustics*. Springer Science & Business Media.
- Shih, S H, D R Hixon, and Reda R Mankbadi. 1997. "Zonal Approach for Prediction of

- Jet Noise.” *Journal of Propulsion and Power* 13 (6): 745–52.
- Singer, Bart A, Kenneth S Brentner, David P Lockard, and Geoffrey M Lilley. 2000. “Simulation of Acoustic Scattering from a Trailing Edge.” *Journal of Sound and Vibration* 230 (3). Elsevier: 541–60.
- Singer, Bart A, David P Lockard, and Kenneth S Brentner. 2000. “Computational Aeroacoustic Analysis of Slat Trailing-Edge Flow.” *AIAA Journal* 38 (9): 1558–64.
- Stoker, Robert W, and Marilyn J Smith. 1993. “An Evaluation of Finite Volume Direct Simulation and Perturbation Methods in CAA Applications.” In *31st AIAA Aerospace Sciences Meeting and Exhibit*. Vol. 1.
- Strawn, Roger C, and Rupak Biswas. 1995. “Computation of Helicopter Rotor Acoustics in Forward Flight.” *Journal of the American Helicopter Society* 40 (3). AHS International: 66–72.
- van der Velden, Wouter C, Stefan Pröbsting, Arjen de Jong, Alexander van Zuijlen, Yaoyi Guan, and Scott Morris. 2015. “Numerical and Experimental Investigation of a Beveled Trailing Edge Flow and Noise Field.” In *21st AIAA/CEAS Aeroacoustics Conference*, 2366.
- Visbal, Miguel R, P E Morgan, and D P Rizzetta. 2003. “An Implicit LES Approach Based on High-Order Compact Differencing and Filtering Schemes.” *AIAA Paper* 4098: 2003.
- Williams, J E Ffowcs, and David L Hawkings. 1969. “Sound Generation by Turbulence and Surfaces in Arbitrary Motion.” *Philosophical Transactions of the Royal Society of London A: Mathematical, Physical and Engineering Sciences* 264 (1151). The Royal Society: 321–42.